Available online at www.sciencedirect.com
SCIENCE DIRECT®
Journal of Computational Physics 198 (2004) 178–210
JOURNAL OF COMPUTATIONAL PHYSICS
www.elsevier.com/locate/jcp

Airflow structures and nano-particle deposition in a human upper airway model

Z. Zhang, C. Kleinstreuer *

Department of Mechanical and Aerospace Engineering, North Carolina State University, Raleigh, NC 27695-7910, USA

Received 17 August 2003; received in revised form 26 November 2003; accepted 28 November 2003
Available online 20 February 2004

Abstract

Considering a human upper airway model, or equivalently complex internal flow conduits, the transport and deposition of nano-particles in the 1–150 nm diameter range are simulated and analyzed for cyclic and steady flow conditions. Specifically, using a commercial finite-volume software with user-supplied programs as a solver, the Euler–Euler approach for the fluid-particle dynamics is employed with a low-Reynolds-number k–ω model for laminar-to-turbulent airflow and the mass transfer equation for dispersion of nano-particles or vapors. Presently, the upper respiratory system consists of two connected segments of a simplified human cast replica, i.e., the oral airways from the mouth to the trachea (Generation G0) and an upper tracheobronchial tree model of G0–G3. Experimentally validated computational fluid-particle dynamics results show the following: (i) transient effects in the oral airways appear most prominently during the decelerating phase of the inspiratory cycle; (ii) selecting matching flow rates, total deposition fractions of nano-size particles for cyclic inspiratory flow are not significantly different from those for steady flow; (iii) turbulent fluctuations which occur after the throat can persist downstream to at least Generation G3 at medium and high inspiratory flow rates (i.e., $Q_{in} \geqslant 30$ l/min) due to the enhancement of flow instabilities just upstream of the flow dividers; however, the effects of turbulent fluctuations on nano-particle deposition are quite minor in the human upper airways; (iv) deposition of nano-particles occurs to a relatively greater extent around the carinal ridges when compared to the straight tubular segments in the bronchial airways; (v) deposition distributions of nano-particles vary with airway segment, particle size, and inhalation flow rate, where the local deposition is more uniformly distributed for large-size particles (say, $d_p = 100$ nm) than for small-size particles (say, $d_p = 1$ nm); (vi) dilute 1 nm particle suspensions behave like certain (fuel) vapors which have the same diffusivities; and (vii) new correlations for particle deposition as a function of a diffusion parameter are most useful for global lung modeling.

Keywords: Inspiratory flow; Nano-size particle deposition; Human airways; Computational fluid-particle dynamics simulation

* Corresponding author. Tel.: +1-919-515-5261; fax: +1-919-515-7968.
E-mail address: ck@eos.ncsu.edu (C. Kleinstreuer).
URL: http://www.mae.ncsu.edu/research/ck_CFPDlab/index.html.

0021-9991/$ - see front matter © 2004 Elsevier Inc. All rights reserved.
doi:10.1016/j.jcp.2003.11.034

1. Introduction

Nano-particles, or ultrafine particles with $d_p < 1$ μm, are encountered in the ambient air and at the workplace, or are generated by inhalers as drug aerosols for therapeutic purposes. These airborne particles or drug aerosols are inhaled through the extrathoracic and tracheobronchial airways down into the alveolar region. A certain percentage may deposit by touching the moist airway surfaces in various lung regions and hence are available for interactions with pulmonary tissue [1]. As a result, toxic particles may induce pulmonary and other diseases [2,3], while drug aerosols may be absorbed to combat diseases. Moreover, studies over the last decade have confirmed that many particles in the nanometer range (actually less than 100 nm) are more harmful than large, respirable particles made of the same material [2,4–7]. However, the exact mechanisms of lung injuries by nano-particles are still being explored. Hence, detailed analyses of nano-particle transport phenomena in the human respiratory tract are needed for a better understanding of the fluid-particle dynamics, and to provide more useful information for health risk assessment or drug aerosol impact studies.

There are relatively few investigations of nano-particle deposition in the human airways, primarily because of the difficulty of nano-particle generation for experimental measurements and accurate predictions with computational fluid-particle dynamics (CFPD) simulations. In a series of papers, Cheng et al. [8–12] reported their measurements of mass transfer and deposition of ultrafine particles ($3.6 < d_p < 150$ nm) in a human nasal and oral airway cast; Cohen et al. [13] and Li et al. [14] reported their experimental work on nano-particle and iodine vapor deposition in an upper tracheobronchial airway cast. For numerical simulations, the transport of nano-particles in an air stream can be considered as a "two-phase flow" problem, for which the basic modeling approaches have been recently analyzed by Kleinstreuer [15]. Fortunately, particle suspensions in human airways can be considered to be dilute due to the low mass loading ratio at the oral/nasal inlet, i.e., one-way coupling is assumed between airflow and particle transport. Both Eulerian and Lagrangian approaches are usually employed to model the transport of nano-particles in airways after the flow fields have been established. As for the Eulerian approach, the particle transport is described by the convection–diffusion equation. Examples include simulations by Yu et al. [16,17], Kimbell et al. [18], and Kepler et al. [19]. Specifically, Yu et al. [16,17] simulated the ultrafine particle diffusion in a single bifurcation airway model and a human upper airway model from mouth/nose to the first two generations of the tracheobronchial tree. Kimbell et al. [18] and Kepler et al. [19] in their numerical analysis parts used a commercial software to simulate the gas transport patterns within nasal airways of a rat and a rhesus monkey, respectively. In the Euler–Lagrange approach, the particle transport is simulated using trajectory equations including random displacement of particles due to Brownian motion. Specifically, Balásházy et al. [20,21] simulated the deposition of 10 nm particles in Generations 3 and 4 of the Weibel model [22]; Asghraiam and Anjilvel [23] calculated the deposition efficiency of 100 nm particles in Generations 16 and 17 of the Weibel model. Recently, Moskal and Gradon [24] simulated the deposition of particles with diameters of 10 and 100 nm in the first two bifurcations of the human respiratory system. However, the k–ϵ model which they employed to simulate the airflow field may overpredict the turbulence effects [25]. Hofmann et al. [26] computed the inspiratory deposition efficiencies of ultrafine particles with $1 \leqslant d_p \leqslant 500$ nm in airway Generations 3 and 4 for different inlet flow rates. The theoretical as well as experimental studies describing the diffusional deposition in the tracheobronchial airways assumed uniform or parabolic inlet velocity profiles and particle distributions. However, the actual velocity profiles and particle distributions are quite different from those axisymmetric profiles and distributions due to flow development and non-uniform particle transport in the upstream airway section. In addition, many published numerical simulations were lacking detailed model validations; for example, the simulated deposition efficiency in a single bifurcation by Yu et al. [16] appears to be unreasonable. Hence, there is a need for more accurate, systematic studies of nano-particle deposition in the human airways under realistic inlet conditions.

The understanding of airflow structures in the human airways underlies the basis for analyzing particle transport and deposition. Steady and transient inspired air flows in the human bronchial airways have been

extensively investigated, both experimentally and theoretically (e.g., [27–41]) and reviewed by Pedley [42] and Grotberg [43,44], among others. Most experimental and computational analyses focused on the mid-size bifurcating airways (e.g., G3–G5) assuming laminar flow. However, at moderate to high breathing rates, the air flow in the larynx and directly below is transitional-to-turbulent which may complicate flow structures as well as aerosol transport and deposition [45].

Steady airflow and micro-particle deposition in the oral airways have also been extensively investigated (see [46–53] among others); however, very little information is available regarding nano-particle transport and deposition during cyclic flow in the human upper airways. The study by Renotte et al. [54] is an exception. They simulated three-dimensional, oscillatory flow through a human larynx model during low-level breathing. However, they did not consider the upper part of the oral airway (i.e., oral cavity and pharynx region) nor particle transport.

While our previous efforts focused on laminar airflow and micro- or nano-size particle transport/deposition in mid-size airways (e.g., G3–G5 or G3–G6) [30,41,55], as well as steady, laminar-transitional-turbulent airflow and micro-particle deposition in an oral airway model [25,45,53], this paper presents transient, laminar-to-turbulent airflow and nano-size particle transport/deposition in a human upper airway model covering mouth inlet to generation G3. Specifically, the contributions of this paper include: (i) cyclic inhalation to analyze transient effects on laminar-transitional-turbulent airflow and nano-particle deposition; and (ii) laminar-to-turbulent airflow as well as transport and deposition of nano-particles, $1 \leqslant d_p \leqslant 150$ nm, in the tracheobronchial airway model G0 (trachea) to G3 under *equivalent* steady inspiratory flow conditions and inlet conditions adjusted from the upstream oral airway model. The quantitative results are of interest to researchers either conducting health risk assessment studies for inhaled toxic particulate matter or analyzing drug aerosol inhalation and deposition at desired lung target sites.

Although this paper stresses fluid flow and nano-particle deposition in the human upper airways, the present methodology, including submodels and solution method, are also applicable to ultrafine particle or vapor transport in curved pipes, obstructed tubes, or branching conduits which appear in many physical, geological, chemical and biological systems.

2. Theory

2.1. Upper airway geometry

As shown in Fig. 1, the present upper airway model consists of two parts: the oral airways, including oral cavity, pharynx, larynx and trachea, as well as a symmetric triple bifurcation representing Generations G0 (trachea) to G3. The dimensions of the oral airway model were adapted from a human cast as reported by Cheng et al. [10]. Variations to the actual cast include a short mouth inlet with a diameter of 2 cm, a modified soft palate, and a strong bend. The dimensions of the four-generation airway model are similar to those given by Weibel [22] for adults with a lung volume of 3500 ml. The airway conduit is assumed to be smooth and rigid. The effects of cartilaginous rings [56], which may appear especially in the trachea, and out-of-plane bifurcations have not been considered in the present analysis. Although most bronchial bifurcations are somewhat asymmetric [57,58] and non-planar, some studies [29,34] have shown that inspiratory flow in an asymmetric bifurcation exhibits the main features of the symmetric case. Non-planar geometries only influence the flow in downstream bifurcations [28,41]. For inspiration, the air and particle flow fields in the non-planar configuration resemble those in the planar configuration, but rotated to some degree and merged with the symmetric secondary vortices [41]. Therefore, the present results, based on the symmetric branching geometries may be extrapolated to the asymmetric branching case with the corresponding local flow rate or non-planar geometries with corresponding rotations.

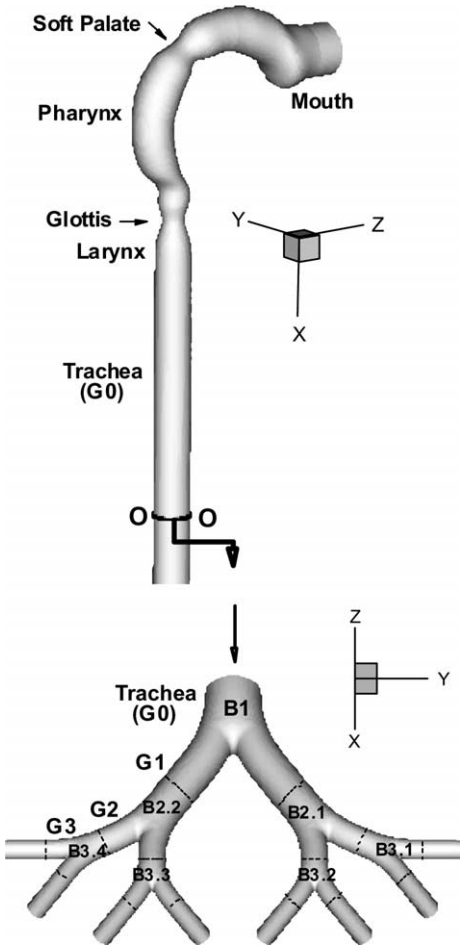

Fig. 1. 3-D views of the oral airway model and bifurcation airway model (generations G0–G3). B1 – first bifurcation, B2.1 and B2.2 – second bifurcation, B3.1, B3.2, B3.3 and B3.4 – third bifurcation (the dashed lines indicate the segmental boundaries).

2.2. Breathing pattern

For cyclic inhalation simulations, a typical flow input waveform [59] representing normal breathing for light activities (see Fig. 2) was used. Its kinematic data at the oral inlet is summarized in Table 1. An intermittent zero-flow period between two inspiratory cycles is employed to replace the expiratory phase because the present analyses only focuses on the transport/deposition of inhaled particles. The complete breathing cycle and different breathing patterns will be considered in future works.

2.3. Governing equations

2.3.1. Airflow

In order to capture the air flow structures in the laminar-to-turbulent flow regimes, i.e., $0 < Re_{\text{local}} < 10^4$ for the present airway configuration and typical inhalation rates, the low-Reynolds-number (LRN) k–ω

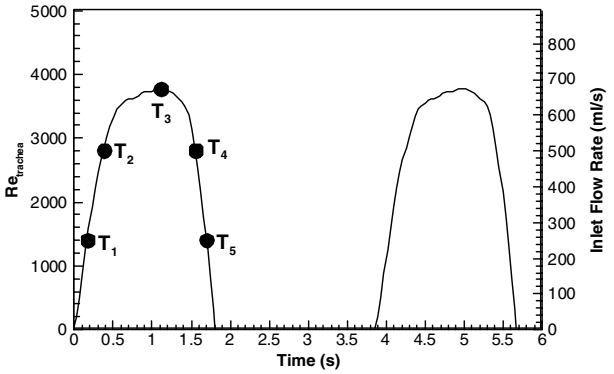

Fig. 2. A typical flow input waveform for light activity breathing with locations of selected time levels.

Table 1
Kinematic data of the representative inhalation waveform (cf. Fig. 2)

Physical parameters	Tidal volume (ml)	Time ratio of inspiratory phase (t_{in}/t_{total})	Breathing frequency (cycle/min)	Womersley number in trachea[a]	Mean Reynolds number in trachea[b]	Peak Reynolds number in trachea
Light activity	907	0.46	15.5	2.25	2800	3770

[a] Womersley number $\alpha = r_0\ (\omega_0/\nu)^{1/2}$, where r_0 is the tube radius, ω_0 is the angular frequency, and ν is the air kinematic viscosity.
[b] Reynolds number $Re = UD/\nu$, where U is the mean velocity and D is the tube diameter.

model of Wilcox [60] was selected and adapted. Zhang and Kleinstreuer [25] demonstrated that it is appropriate for such internal laminar-to-turbulent flows. In general, the transport equations in tensor notation, implying the double-index summation convention, read:

Continuity equation:

$$\frac{\partial u_i}{\partial x_i} = 0. \tag{1}$$

Momentum equation:

$$\frac{\partial u_i}{\partial t} + u_j \frac{\partial u_i}{\partial x_j} = -\frac{1}{\rho}\frac{\partial p}{\partial x_i} + \frac{\partial}{\partial x_j}\left[(\nu + \nu_T)\left(\frac{\partial u_i}{\partial x_j} + \frac{\partial u_j}{\partial x_i}\right)\right]. \tag{2}$$

Turbulent kinetic energy (k) equation:

$$\frac{\partial k}{\partial t} + u_j \frac{\partial k}{\partial x_j} = \tau_{ij}\frac{\partial u_i}{\partial x_j} - \beta^* k\omega + \frac{\partial}{\partial x_j}\left[(\nu + \sigma_k \nu_T)\frac{\partial k}{\partial x_j}\right]. \tag{3}$$

Pseudo-vorticity (ω) equation:

$$\frac{\partial \omega}{\partial t} + u_j \frac{\partial \omega}{\partial x_j} = \alpha\frac{\omega}{k}\tau_{ij}\frac{\partial u_i}{\partial x_j} - \beta\omega^2 + \frac{\partial}{\partial x_j}\left[(\nu + \sigma_\omega \nu_T)\frac{\partial \omega}{\partial x_j}\right]. \tag{4}$$

For convenience, summation notation is used with $i, j = 1, 2, 3$, where u_1, u_2, u_3 and x_1, x_2, x_3 are the x, y, z components of the velocity vector and the spatial coordinate vector, respectively. The symbols in the above

equations, t, ρ, p, ν, τ_{ij} k and ω are time, density, pressure, kinetic molecular viscosity, Reynolds stress tensor, turbulence kinetic energy, and dissipation per unit turbulence kinetic energy, respectively; ν_T is the turbulent viscosity given as $\nu_T = c_\mu f_\mu k/\omega$, and the function f_μ is defined as $f_\mu = \exp[-3.4/(1 + R_T/50)^2]$ with $R_T = \rho k/(\mu\omega)$ while μ is the dynamic molecular viscosity ($\mu = \rho\nu$); C_μ, α, β, β^*, σ_k, and σ_ω are turbulence constants, i.e.,

$$C_\mu = 0.09, \quad \alpha = 0.555, \quad \beta = 0.8333, \quad \beta^* = 1, \quad \sigma_k = \sigma_\omega = 0.5. \tag{5a–f}$$

The associated boundary conditions include uniform velocity profiles prescribed at the mouth inlet, and uniform pressure at the outlets. For cyclic inspiratory flow simulations, the mean inlet velocities are calculated from the instantaneous flow rates following the given input pulse. Three cycles were simulated to avoid start-up effects on the air-particle flow fields. A long exit tube that extends about nine tube diameters from the end of the trachea was used in the oral airway model to eliminate the influence of the zero-pressure assumption at the outlet. However, because the actual length from the glottis to the first carina in the trachea is about 14 cm, the mean-velocity field, turbulence quantities, and mass fraction distributions in the trachea at about 11 cm from the glottis, were adjusted as the inlet conditions of the bifurcating airway segment (i.e., Generations G0–G3) (see Fig. 1). The first parent tube length of the bifurcation airway model is about 3 cm. Necessary adjustments included: (1) the magnitudes of velocity and turbulence quantities which were recalculated due to the slight variation in trachea diameter ($D = 1.37$ cm) and Weibel's lung model ($D = 1.6$ cm); and (2) the profiles of variables were also reconstructed for the inlet to the bronchial airways, G0–G3, employing an inverse distance interpolation weighting method after Shepard [61].

At the mouth inlet, the initial values for k, and ω were assigned using the following empirical relation [62]

$$k = 1.5(I \times u_{in})^2 \quad \text{and} \quad \omega = \frac{k^{0.5}}{0.6R}, \tag{6}$$

where I is the turbulence intensity usually taken as 0.037 and R is the radius of the inlet tube.

2.3.2. Mass transfer of nano-particles

The convection–diffusion mass transfer equation of nano-particles, where the dominant transfer mechanisms are Brownian motion and turbulent dispersion, can be written as

$$\frac{\partial Y}{\partial t} + \frac{\partial}{\partial x_j}(u_j Y) = \frac{\partial}{\partial x_j}\left[\left(\tilde{D} + \frac{\nu_T}{\sigma_Y}\right)\frac{\partial Y}{\partial x_j}\right]. \tag{7}$$

Here Y is the mass fraction of nano-particles and $\sigma_Y = 0.9$ is the turbulence Prandtl number for Y. The effective aerosol diffusion coefficient ($\tilde{D}$) is calculated as follows [12,63]:

$$\tilde{D} = (k_B T C_{slip})/(3\pi\mu d_p), \tag{8}$$

where k_B is the Boltzmann constant (1.38×10^{-23} J K^{-1}); T is the temperature; d_p is the particle diameter; and C_{slip} is the Cunningham slip correction factor:

$$C_{slip} = 1 + \frac{2\lambda_m}{d_p}\left[1.142 + 0.058\exp\left(-0.999\frac{d_p}{2\lambda_m}\right)\right], \tag{9}$$

where λ_m is the mean free path in air. The diffusivities of selected particles in the nano-size range determined by Eq. (8) are given in Table 2. The diffusivities for vapors of some species (most are the components of

Table 2
Diffusivities ($\tilde{D}$) of nano-particles

Particle diameter (nm)	1	3	5	10	20	30	50	100	150
Diffusivity (cm^2/s)	5.34×10^{-2}	5.95×10^{-3}	2.15×10^{-3}	5.44×10^{-4}	1.39×10^{-4}	6.32×10^{-5}	2.38×10^{-5}	6.76×10^{-6}	3.15×10^{-6}

Table 3
Diffusivities ($\tilde{D}$) of some vapors in air [64]

Vapors	Naphthalene	Benzanthracene	*n*-Octane	*n*-Decane	1-Methyl-3-ethylbenzene
Diffusivity (cm^2/s)	5.90×10^2	5.10×10^2	5.98×10^2	5.00×10^2	5.65×10^2

fuels, see [64]) are approximately to that of 1 nm particles (see Table 3); hence, their transport and deposition may behave similarly. Moreover, the present methodology and qualitative results are also applicable to transport and deposition of vapors with other different diffusivities.

The local wall mass flux of nano-particles can be determined as

$$\dot{m}_{\mathrm{w}} = -\rho A_i \left(\tilde{D} + \frac{\nu_{\mathrm{T}}}{\sigma_Y} \right) \frac{\partial Y}{\partial n}|_i, \tag{10}$$

where A_i is the area of local wall cell (i), and n is the direction normal to the wall. The local deposition fraction (DF) of nano-particles, which is defined as the ratio of local wall mass flux to the inlet mass flux, can be expressed as

$$\mathrm{DF}_{\mathrm{local}} = \left[-A_i \left(\tilde{D} + \frac{\nu_{\mathrm{T}}}{\sigma_Y} \right) \frac{\partial Y}{\partial n}|_i \right] / (Q_{\mathrm{in}} Y_{\mathrm{in}}) \tag{11}$$

and the regional DF can be determined as

$$\mathrm{DF}_{\mathrm{region}} = \sum_{i=1}^{n_{\mathrm{w}}} \left[-A_i \left(\tilde{D} + \frac{\nu_{\mathrm{T}}}{\sigma_Y} \right) \frac{\partial Y}{\partial n}|_i \right] / (Q_{\mathrm{in}} Y_{\mathrm{in}}), \tag{12}$$

where n_{w} is the number of wall cells in one specific airway region, e.g., oral airway, first airway bifurcation, etc., while Q_{in} and Y_{in} are the flow rate and mass fraction at the mouth, respectively. The local deposition patterns of nano-particles can be quantified in terms of a deposition enhancement factor (DEF) (cf. [65,66]), which is defined as the ratio of local to average deposition densities, i.e.,

$$\mathrm{DEF} = \left[\left(\tilde{D} + \frac{\nu_{\mathrm{T}}}{\sigma_Y} \right) \frac{\partial Y}{\partial n}|_i \right] \Bigg/ \left\{ \sum_{i=1}^{n_{\mathrm{w}}} \left[A_i \left(\tilde{D} + \frac{\nu_{\mathrm{T}}}{\sigma_Y} \right) \frac{\partial Y}{\partial n}|_i \right] \Bigg/ \sum_{i=1}^{n_{\mathrm{w}}} A_i \right\}. \tag{13}$$

DEF indicates particle deposition "hot spots" in a given region.

Assuming that the airway wall is a perfect sink for aerosols upon touch, the boundary condition on the wall is $Y_w = 0$. This assumption is reasonable for fast gas/aerosol-wall reaction kinetics [67] and also suitable for evaluating particle deposition on lung airway surfaces which act as perfectly absorbing walls.

3. Numerical method

The numerical solutions of the continuity and momentum equations as well as the k, ω, and mass transfer equations were carried out with a user-enhanced commercial finite-volume based program, i.e., CFX4.4 from AEA Technology [62]. The numerical program uses a structured multiblock discretization scheme with body-fitted coordinates. In the present simulation, the pressure implicit splitting of operators (PISO) algorithm with under-relaxation was employed to solve the flow equations [68]. All variables, including velocity components, pressure, and turbulence quantities, are located at the centroids of the control volumes. An improved Rhie–Chow interpolation method was employed to obtain the velocity components, pressure and turbulence variables on the control volume faces from those at the control volume centers. A higher-order upwind (HUW) differencing scheme, which is second-order accurate in space, was used to model the advective terms of the transport equations. A fully implicit first-order backward difference with an adaptive time steps ($0.001 \leqslant \Delta t \leqslant 0.01$ s) was used for temporal discretization in cyclic flow simulation. The sets of linearized and discretized equations for all variables were solved using the Block Stone's method.

The computational mesh was generated with CFX Build4, where the near-wall region requires a very dense mesh. Specifically, the thickness of the near-wall cells was chosen to fully contain the viscous sublayers and to resolve any geometric features present there. As a requirement of LRN turbulence modeling, the first grid point above the wall was given a value of $y^+ \leqslant 1$, where $y^+ = u_\tau y/\nu$ is the inner variable or sublayer-scaled distance with u_τ being the friction velocity ($u_\tau \equiv \sqrt{\tau_w/\rho}$, where τ_w is the wall shear stress). This criterion is strictly maintained for all computations. The mesh topology was determined by refining the mesh until grid independence of the solution of flow and mass fraction fields as well as particle deposition was achieved. The mesh independence of the DEF is also examined. For example, Fig. 3 shows the maximum DEF in the oral airway model for different nano-size particles at $Q_{in} = 30$ l/min for two different grid configurations. The calculation of DEF depends on the surface mesh size as described in Eq. (13). The

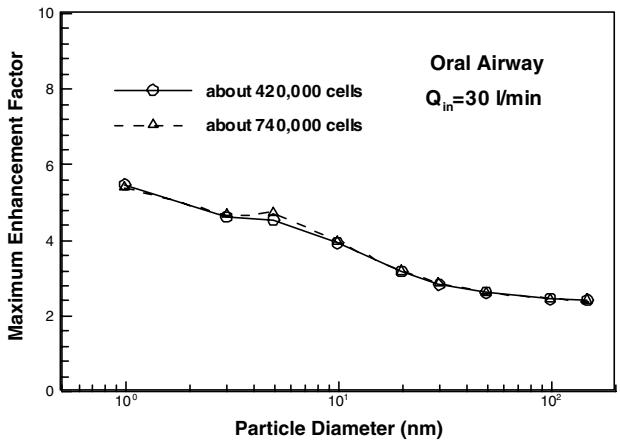

Fig. 3. Grid refinement test for the distributions of the deposition enhancement factor of nano-particles in the oral airway model for steady inhalation ($Q_{in} = 30$ l/min).

minimum, average and maximum surface cell areas for the denser mesh case (~740,000 cells) are about 0.12, 0.45, and 1.17 mm^2, respectively; while they are about 0.217, 0.809 and 2.07 mm^2 for the coarse mesh case (~420,000 cells), respectively. Calculations with grids consisting of about 740,000 cells show negligible differences (within 3%) in the maximum DEF, when compared to simulations with a mesh containing about 420,000 cells. However, the computational time for the fine mesh case (~740,000 cells) is approximately 4 times longer than for the coarse mesh case (~420,000 cells). The final mesh contains about 420,000 and 670,000 cells for the oral airway and four-generation airway model, respectively. The minimum, average and maximum surface mesh size for the four-generation airway model are about 0.034, 0.23, and 0.85 mm^2, respectively. The computations were performed on an SGI Origin 2400 workstation with 32 GB RAM and multiple 450 MHz CPUs. The solution of the flow field at each time step was assumed to be converged when the dimensionless mass residual was negligible, i.e., (total mass residual)/(mass flow rate) $< 10^{-3}$. The convergence of other variables was monitored as well. Typical run times for the fluid flow and mass transfer simulations on eight processors with parallel algorithm was approximately 24–65 h for the oral airway model and 8 h for the four-generation model under steady inhalation condition and 150 h for the oral airway model during one inspiratory cycle.

4. Model validations

The present CFPD model has been successfully validated with various experimental data sets for steady and transient laminar flows in bifurcations [30,41] and for laminar, transitional and turbulent flows in tubes with local obstructions [25,45].

The current simulation approach for the deposition of nano-particles due to diffusional transport has been validated with both analytical solutions in straight pipes, experimental data for a double bifurcation airway model (see [55]) and experimental data in an oral airway model [69]. For example, computer simulation results of steady nano-particle deposition in a straight pipe with both uniform inlet velocity and particle concentration profiles were compared with analytical expressions given by Ingham [70], as shown in Fig. 4. Fig. 5 provides nano-particle deposition results for different inlet Reynolds numbers in a double bifurcation model representing Generations G3–G5 of Weibel's lung model. In comparison, experimental data points of Kim [71] confirm the deposition trend in each bifurcation, although the laboratory results did

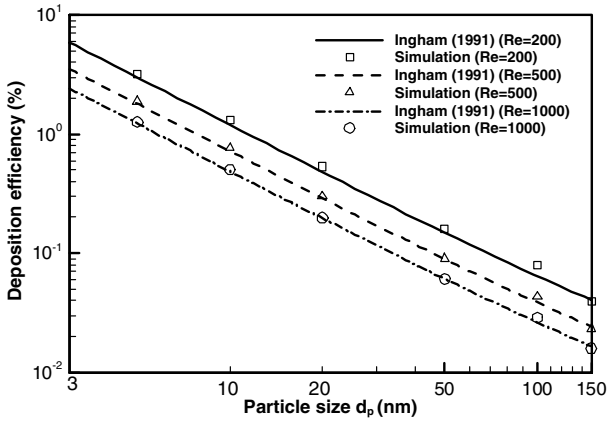

Fig. 4. Ultrafine particle deposition efficiencies in a straight pipe with uniform inlet velocity and particle concentration profiles as a function of particle diameter d_p.

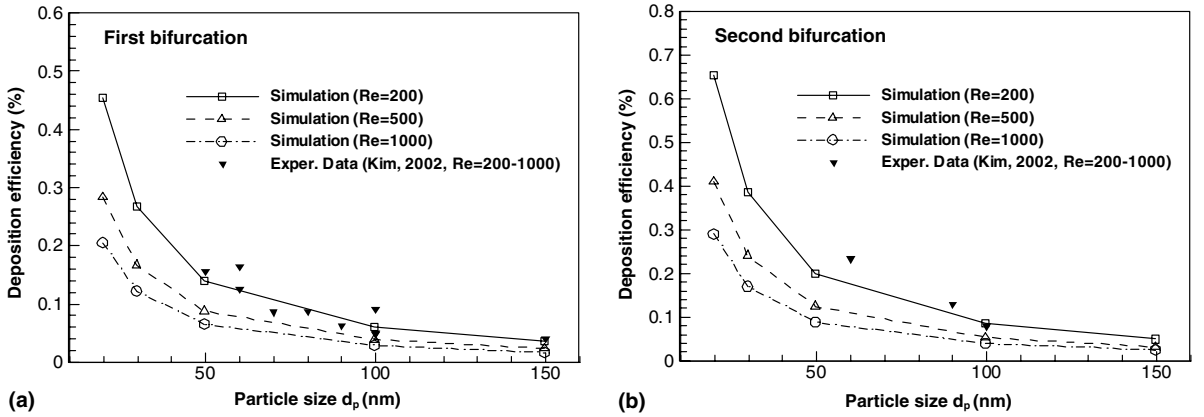

Fig. 5. Comparison of the simulated deposition efficiencies of nano-particles in a double bifurcation model with the experimental data of Kim [71] for: (a) first bifurcation; and (b) second bifurcation.

not reveal any Reynolds number effects. The discrepancies may be attributed to slight differences in geometries as well as (unreported) experimental uncertainties.

In summary, the good agreements between independent observations and numerical predictions instill confidence that the present computer simulation model is sufficiently accurate to analyze laminar-to-turbulent air flow as well as nano-particle transport and deposition in three-dimensional oral and bifurcating airways.

5. Results and discussion

5.1. Airflow and particle deposition in the oral airway model for cyclic inhalation

The relative importance of unsteadiness in laminar, oscillatory flow can be expressed with the Womersley number ($\alpha = r_0\sqrt{\omega_0/\nu}$) which represents the ratio of unsteady inertial forces to the viscous forces. Generally, it is assumed that unsteadiness is important for $\alpha > 1$ [72]. However, during the major part of the respiratory cycle under normal breathing condition as shown in Fig. 2, the flow may transit from laminar to transitional and turbulent in the trachea. The effect of unsteadiness on turbulent flow can be assessed roughly by evaluating a turbulent counterpart of the Womersley number α^* as proposed by Pedley et al. [72]. Specifically, α^* can be computed by replacing ν in α with the eddy viscosity ν_T. Now, considering light-activity breathing as in the present case (see Table 1), α is about 2.25 while α^* does not exceed 0.7 in the trachea. The relatively small α^*-value implies that the presence of turbulent flow may reduce locally the effects of unsteadiness. Thus, focusing on detailed variations of flow fields during normal breathing, the effects of unsteadiness are analyzed as well.

5.1.1. Air flow structures

5.1.1.1. Transient flow effects. Of the simulated transient transitional flow in the oral airway model for light activity breathing, only the results for selected time levels T_1–T_5 (see Fig. 2), which include all the basic flow features, are displayed and discussed.

Fig. 6(a) shows the velocity field in the oral airway model at time level $t = T_1$ during the accelerating phase. The cross-sectional views display the axial velocity contours as well as secondary velocity vectors. The cross sections C–C′, D–D′, E–E′ and F–F are zero, one, three, and six diameter(s) from the glottis,

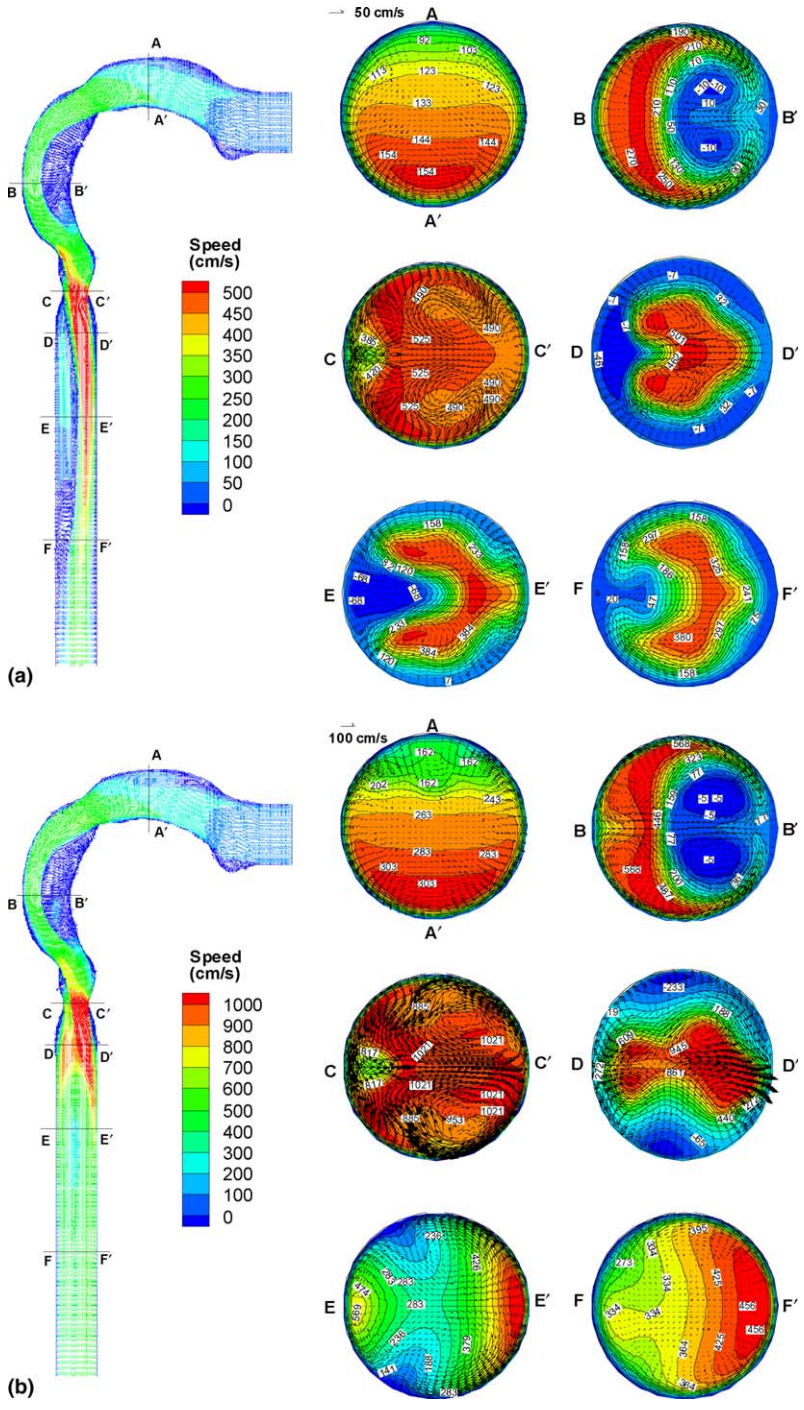

Fig. 6. Velocity profiles in the oral airway model during cyclic inhalation at: (a) $t = T_1$; (b) $t = T_2$; and (c) $t = T_5$. The left panel exhibits side-plane ($y = 0$ plane) velocity contours with uniform velocity vectors. The right panel shows the axial velocity contours (magnitudes in cm/s) and secondary velocity vectors at different cross sections.

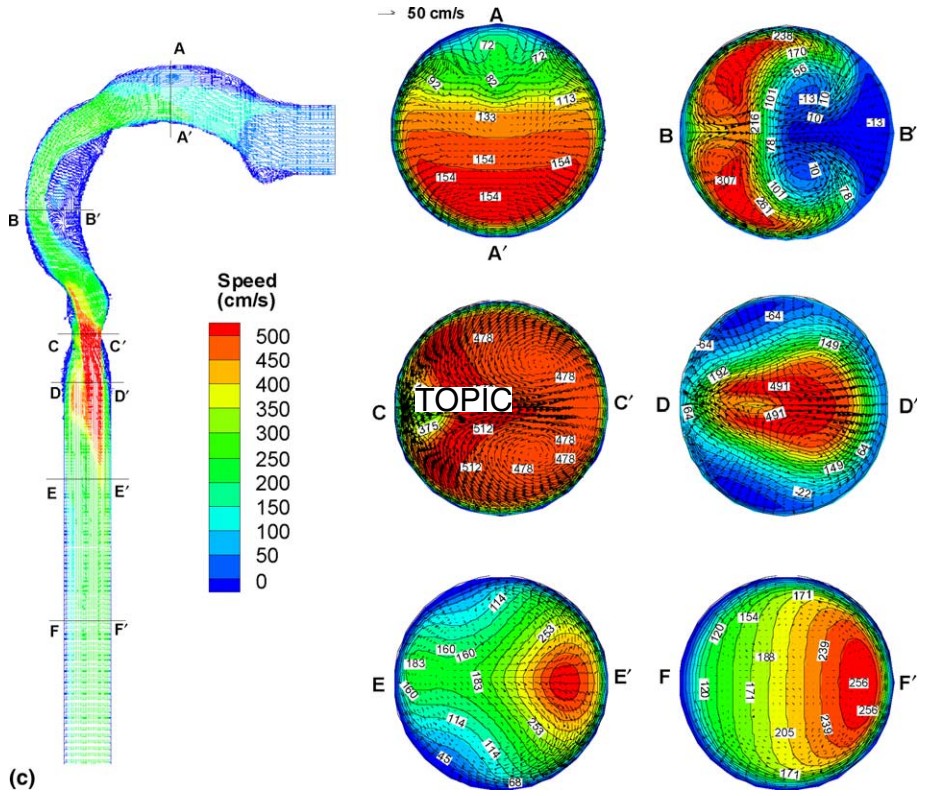

Fig. 6. (*continued*)

respectively. The Reynolds number is about 1400 in the trachea and laminar flow prevails at this time level. Flow separation occurs at the lower portion of the mouth (near the tongue), the inside bend of the pharynx (B–B′), and downstream of the vocal fold (glottis) (D–D′ and E–E′), which are generated due to strong changes in cross-sectional areas. An asymmetric, central jet created by the restriction of the vocal folds can be observed as well. Secondary motion is set up when the flow turns a bend from the mouth to the pharynx because of the centrifugally induced pressure gradient. Two distinct vortices appear at cross section B–B′. Secondary flows become somewhat more complicated downstream from the glottis when the air stream encounters a large expansion or constriction with the variation of cross-sectional areas and continues to turn a bend from the pharynx to the larynx. The intensity of secondary flow decreases with further flow development downstream in the trachea.

At $t = T_2$, the flow may transit from laminar to turbulent, and hence the velocity profiles change measurably (see Fig. 6(b)). In the oral entrance regions (cf. cross section A–A′) the velocity profiles are similar to those at $t = T_1$, except for the increase of secondary motion and two additional secondary vortices appearing at A–A′. Turbulence fluctuations are still weak in this section. However, after the soft palate (cf. Fig. 1) both axial and secondary flows change significantly with the transition to turbulence. The length of the separated flow zone after the glottis also decreases compared to that at $t = T_1$. For example, at $t = T_2$ there is no reverse flow at cross section E–E′, i.e., three diameters downstream of the glottis, while it still appears at $t = T_1$. This may be because the occurrence of transition to turbulence in the downstream regions of the shear layer modifies the location of reattachment compared with that for laminar flow. With further redistribution of the kinetic energy of the flow over most of the cross section, the velocity profiles become

more blunt from the left to the right wall, and the maximum velocity zone moves to the anterior wall (F′) at the cross section F–F′. The secondary motion decays and appears very weak at this cross section. As time progresses and the volumetric flow rates increase, the turbulent flow features become more pronounced, and at peak flow ($t = T_3$) the flow structures are similar to those of steady flow at the same Reynolds number, as discussed by Kleinstreuer and Zhang [45].

Transient effects can be clearly seen when comparing the velocity profiles in the decelerating phase at $t = T_5$ (see Fig. 6(c)) to those at the accelerating phase $t = T_1$ in Fig. 6(a) at the same Reynolds number. Specifically, when compared to flow fields at $t = T_1$, a reduced length of the recirculating zone in the trachea is observed at $t = T_5$, shifting the maximum axial velocity at sections E–E′ and F–F′ as well as the blunt profiles from the left to the right wall at section F–F′. It should be noted that the flow at $t = T_5$, i.e., during deceleration exhibits apparent turbulent features after the glottis, which may be attributed to lingering flow effects and the core flow being less influenced by the boundary layers under the cyclic inspiratory flow condition.

5.1.1.2. Turbulence intensity aspects. The variation of the turbulence intensity ($\hat{k} = k_{\text{mean}}/u_{\text{avg}}^2$) averaged over cross-sectional areas as a function of the axial distance from the mouth inlet is shown in Fig. 7 for the representative time levels T_1–T_5 and compared to $\hat{k}$ for equivalent steady flows. The u_{avg} is the inlet mean velocity at the mean flow rate $Q_{\text{in}} = 30$ l/min. As expected, at $t = T_1$ when $Re = 1400$, $\hat{k} \approx 0$. At other time levels, turbulent fluctuations are very weak in the oral cavity. However, after the soft palate constriction the turbulence kinetic energy becomes strong, peaks after the glottis, and then decays rapidly, eventually approaches an asymptotic level. The maximum turbulence intensity occurs 2.0–2.5 cm downstream of the glottis, which may vary with the inhalation flow rate. Due to the transient effects, the transition from laminar to turbulent flow during cyclic inhalation cannot be as rapid as in the equivalent steady case. Specifically, at $t = T_2$ during the accelerating phase, turbulence does not occur from the soft palate to glottis as it is the case for steady flow ($Re = 2800$). On the contrary, turbulent fluctuations are still strong for $t = T_4$ during deceleration while they disappear for the equivalent steady case ($Re = 1400$). The turbulence intensities around the soft palate at $t = T_3$ and T_4 under the cyclic inhalation condition are both lower than those for the equivalent steady cases. With further flow developments in the oral airway, the $\hat{k}$-distributions after the glottis at $t = T_2$, T_3, and T_4 are quite similar to those for the equivalent steady flows.

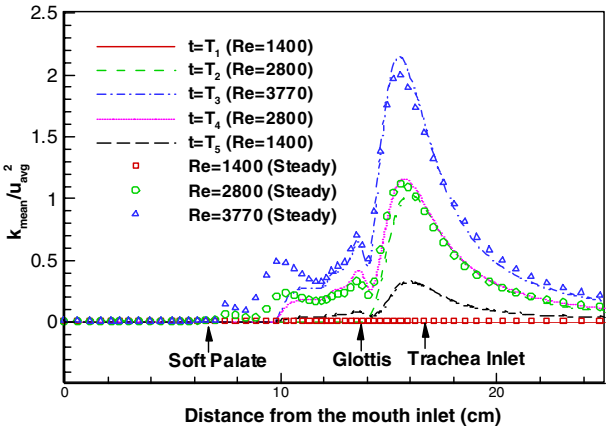

Fig. 7. Variations of cross-sectional area-averaged turbulence kinetic energy in the oral airway model at different time levels during cyclic inhalation.

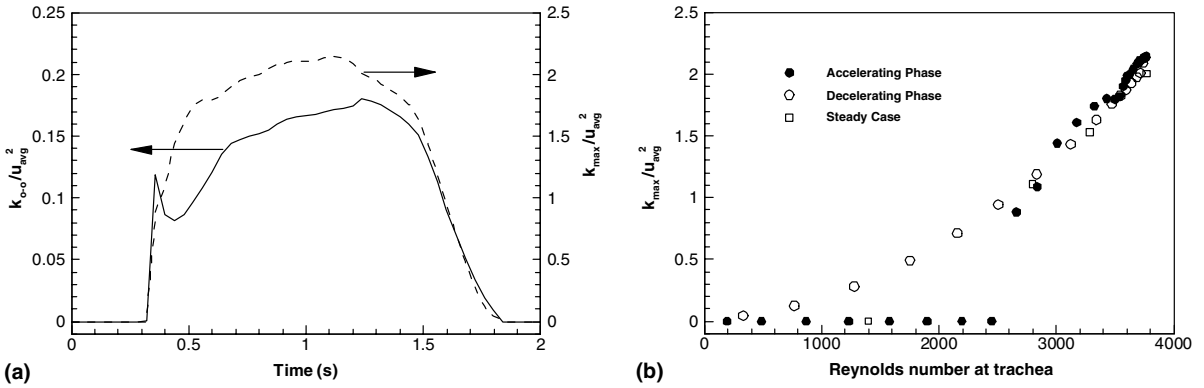

Fig. 8. Variation of turbulence kinetic energy in the oral airway model during one inspiratory cycle with: (a) time; and (b) Reynolds number in the trachea.

The variations of turbulence kinetic energy during one inhalation cycle can be further observed in Fig. 8(a) and (b), where k_{o-o} is the area-averaged kinetic energy at cross section O–O (see Fig. 1), and k_{max} is the maximum, area-averaged turbulence kinetic energy in the oral airway model. The turbulence kinetic energy increases sharply at the time intervals when $Re_{trachea} \approx 2400$ during the accelerating phase, and becomes negligible when $Re_{trachea} < 800$ during deceleration, i.e., a cyclic "turbulence hysteresis" can be observed.

5.1.1.3. Axial pressure profiles. The results of pressure drops as a function of axial distance from the mouth in the oral airway geometry are shown in Fig. 9, where the values at different time levels under cyclic inhalation condition are compared to those for steady flow at equivalent Reynolds numbers. In Fig. 9, Δp is the pressure drop defined as $\Delta p = \bar{p} - p_{in}$, where $\bar{p}$ is the cross-sectional area-averaged pressure and p_{in} is the inlet pressure at the mouth. As expected, the pressure drop in the oral airway increases with flow rate. In both accelerating and decelerating periods, the transient pressure drops from T_1 to T_5 essentially agree with the equivalent steady-state cases, but the differences are somewhat larger during deceleration.

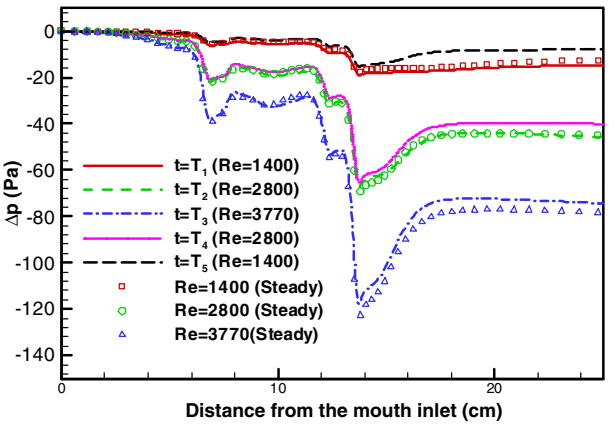

Fig. 9. Variations of pressure drop in the oral airway model at different time levels during cyclic inhalation.

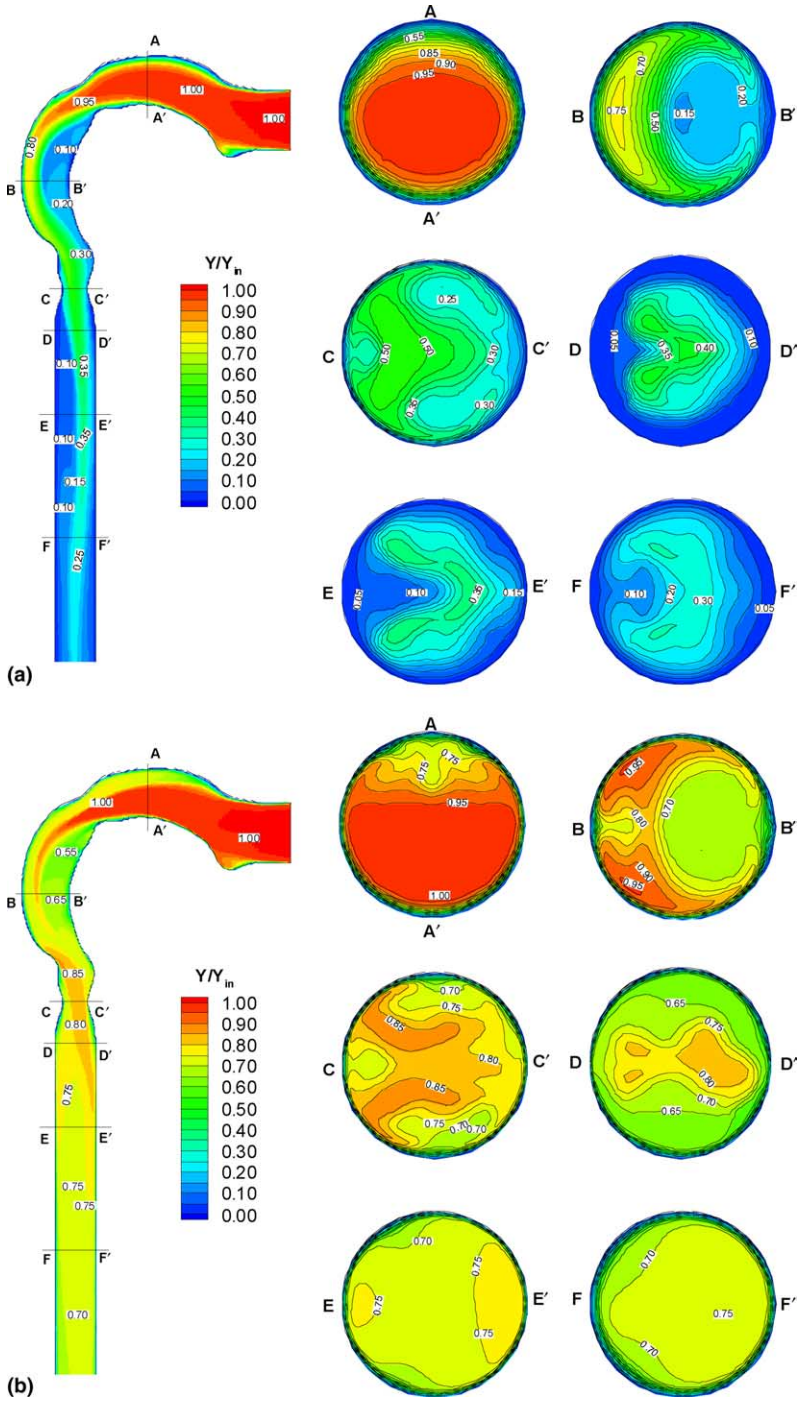

Fig. 10. Concentration contours of nano-particles ($d_p = 1$ nm) in the oral airway model during cyclic inhalation at: (a) $t = T_1$; (b) $t = T_2$; (c) $t = T_3$; and (d) $t = T_5$. The left panels exhibit side-plane ($y = 0$ plane) concentration contours, while the right panels show the concentration distributions at different cross-sectional planes.

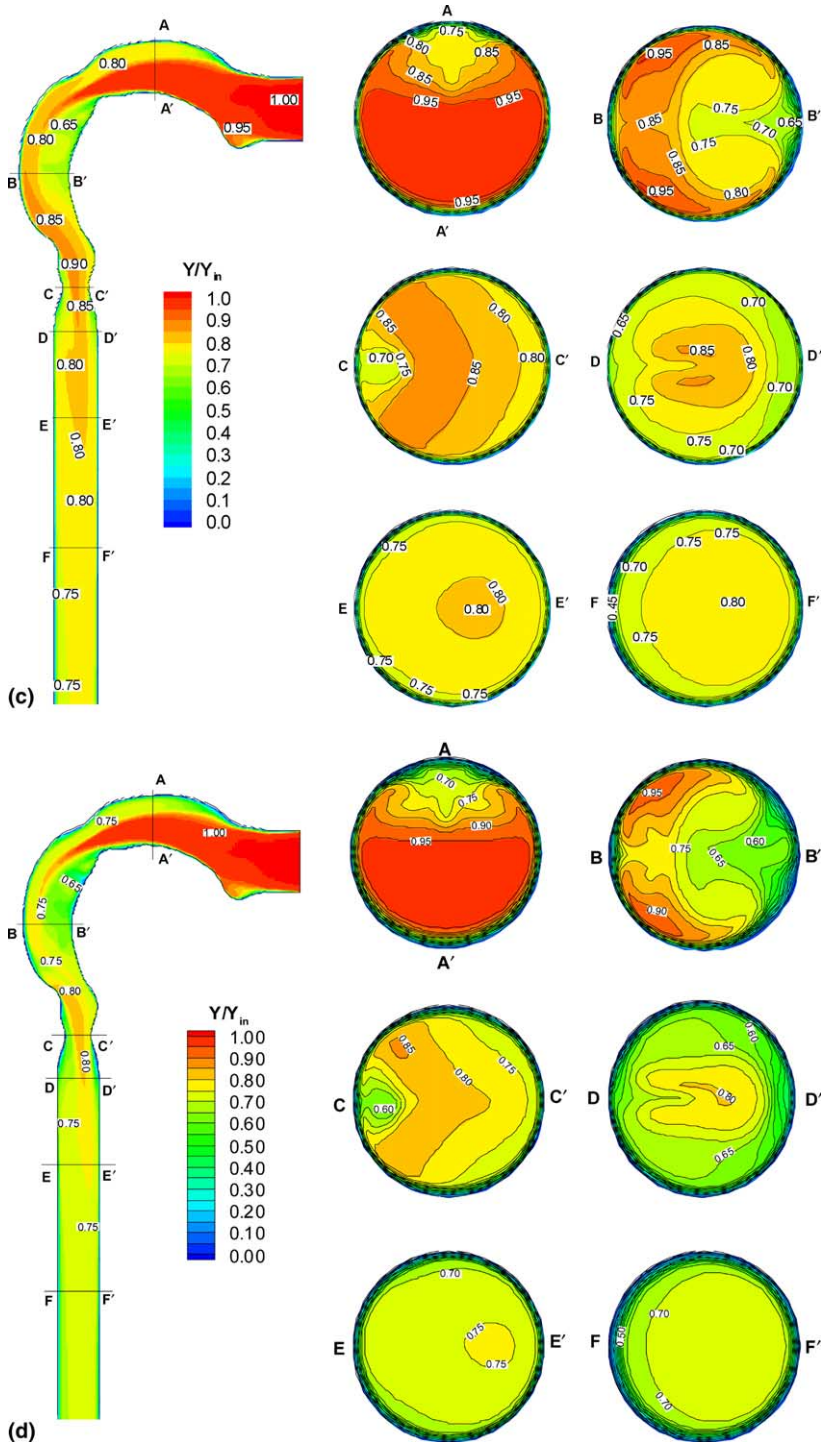

Fig. 10. (*continued*)

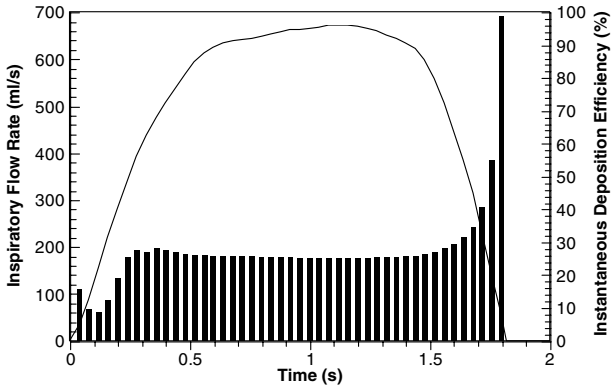

Fig. 11. Instantaneous deposition efficiency of nano-particles ($d_p = 1$ nm) in the oral airways during inspiratory cycle.

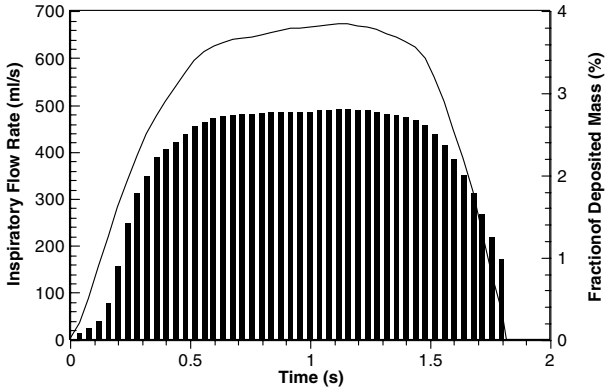

Fig. 12. Mass fractions of deposited nano-particles ($d_p = 1$ nm) in the oral airways during inspiratory cycle.

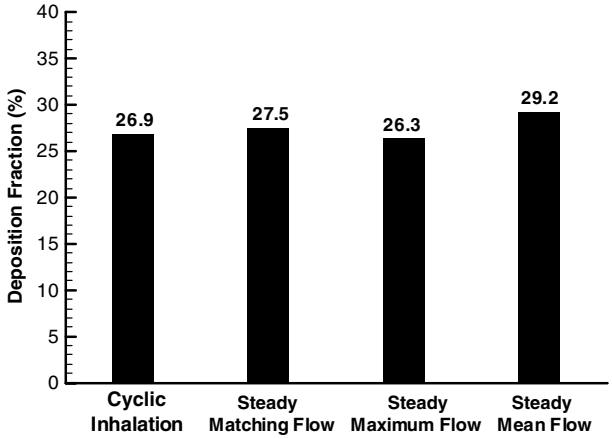

Fig. 13. Comparisons of total deposition fractions of nano-particles ($d_p = 1$ nm) in the oral airway model under cyclic and steady inhalation conditions for different flow rates.

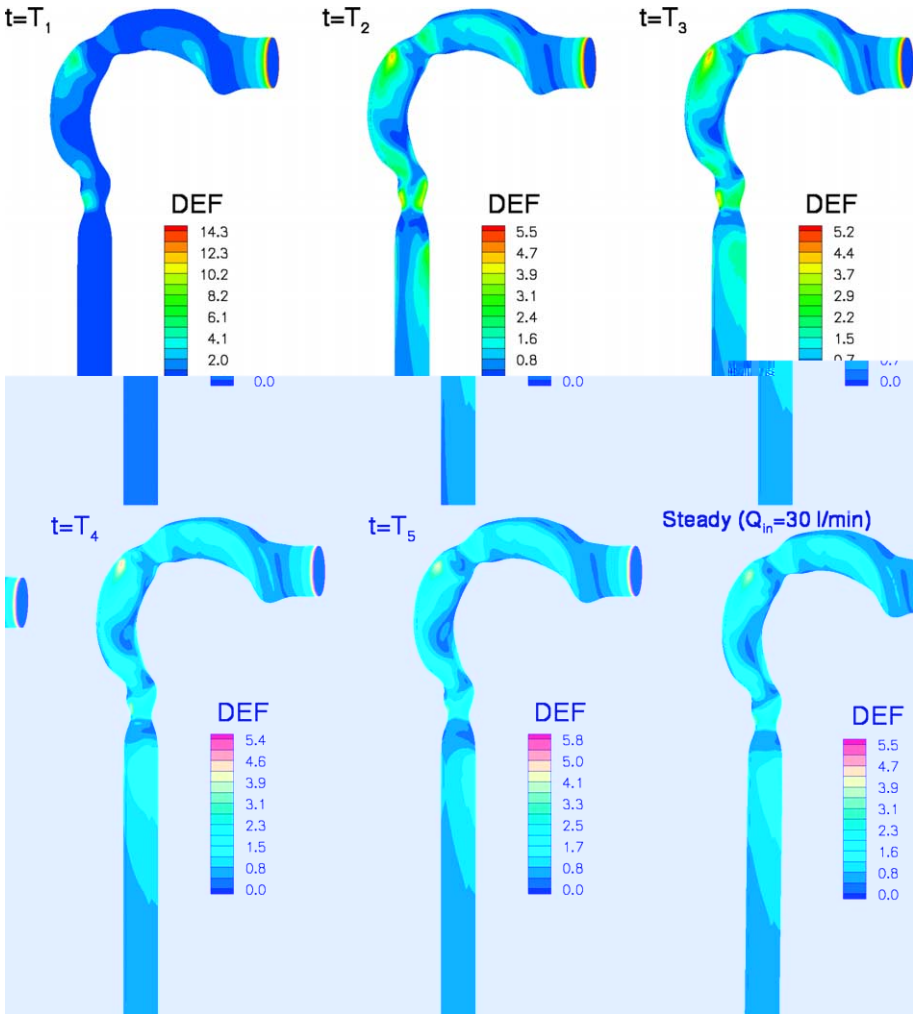

Fig. 14. 3-D distributions of the deposition enhancement factor (DEF) in the oral airway model at different time levels during cyclic inhalation and steady inhalation with $Q_{in} = 30$ l/min.

5.1.2. Nano-particle transport and deposition considering cyclic inhalation

The transient and steady-state fluid-particle dynamics are illustrated and discussed for $d_p = 1$ nm, i.e., $\tilde{D} = 0.053$ cm^2/s which is also representative for some components of fuel vapors in air (see Table 3), in terms of local mass fractions and wall depositions (see Figs. 10–14). Then, DFs for wide ranges of particle diameters $1 \leqslant d_p \leqslant 150$ nm and inhalation flow rates $7.5 \leqslant Q_{in} \leqslant 60$ l/min are presented (see Figs. 15 and 16).

5.1.2.1. Nano-particle ($d_p = 1$ nm) or vapor distributions. The mass fraction contours of 1 nm particles in the oral airway for different time levels, $t = T_1$, T_2, T_3 and T_5 (see Fig. 2) for light-activity breathing are displayed in Fig. 10(a)–(d). A uniform particle concentration, directly related to the instantaneous flow rate condition, was assumed at the mouth inlet. Clearly, lower mass fractions are observed near flow separation, flow stagnation, and in low-velocity zones because mass transfer by convection is relatively low in these

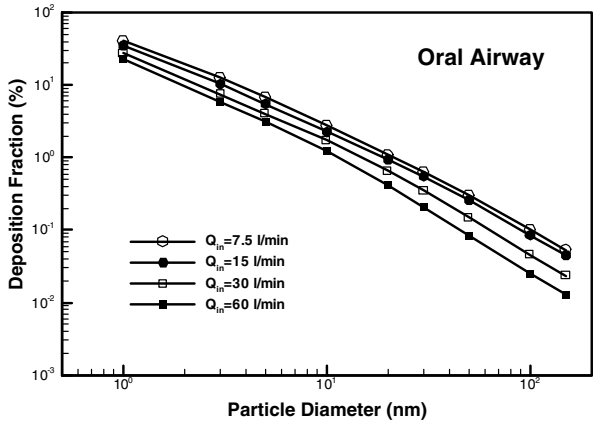

Fig. 15. Nano-particle deposition fractions in the oral airway model vs. flow rate and particle diameter.

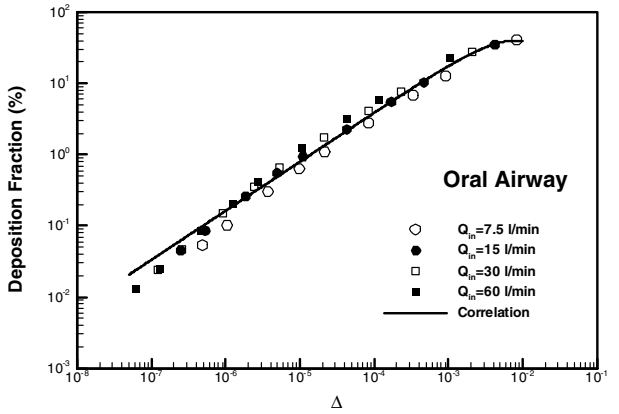

Fig. 16. Nano-particle deposition efficiencies in the oral airway model as a function of diffusion parameter.

regions and even high species concentrations cannot be easily dispersed. The local concentration gradient near the wall indicates the particle deposition rate at that site. Thus, the local deposition rate tends to be high in the oral cavity and low in the trachea due to the species redistributions over the cross sections driven by secondary and reverse flows. At $t = T_1$ (beginning of inspiration), particles have hardly reached the trachea. Due to the existence of the laryngeal jet and flow separation, the maximum concentration regions are located at the center of the tube at cross sections D–D′, E–E′ and F–F′. With increasing flow rates during acceleration ($t = T_2$), transition to turbulent flow may occur, and the situation changes somewhat. The inlet particles are quickly connected to the trachea, undergoing rapid mixing. Affected by the free airstreams, the concentration fields are very complicated in the mouth-to-pharynx as well as in the larynx regions. But in the trachea (see cross sections E–E′ and F–F′), the species distributions tend to be more uniform due to strong mixing, driven by secondary flows upstream. Even uniformly distributed mass fractions can be observed in the trachea at peak flow, i.e., $t = T_3$ (see Fig. 10(c)). Similar to the airflow structures, the features of concentration fields change very little from $t = T_3$ to T_5 during deceleration (cf. Figs. 10(d) and 6(c)).

Fig. 11 shows the variation of momentary deposition efficiencies during one inhalation cycle, which is defined as the ratio of deposited mass to inhaled mass at a given time level. At the very beginning of inspiration ($t < 0.05$ s), the instantaneous deposition efficiency is higher than during the next time interval because of the presence of lingering particles at the end of the previous inspiration cycle. With the deposition of the remaining particles, the DE decreases a little and then increases from $t = 0.1$–0.3 s with increasing flow rate because particles propagate faster both axially and radially with a higher flow rate due to the convection–diffusion phenomena. The DEs remain almost constant during the major part of the inspiratory cycle (i.e., from $t = 0.3$–1.5 s) with the onset of turbulence. However, from $t = 1.5$ s to the end of inspiration, DE increases with decreasing flow rate because of the increasing residence time for particles. The peak DE can be as high as 99% near the end of inspiration ($t = 1.8$ s) at near-zero flow rate.

With the inhaled mass of nano-particles being proportional to the flow rate, the fraction of depositing particle mass may still decrease even if the momentary deposition efficiency increases near the end of inspiration (see Fig. 12). The fraction of mass deposition is defined as the ratio of momentary deposited mass to the total deposited mass during one inspiratory cycle. Moskal and Gradon [24] stated that an enhancement of deposition was observed during the switch from inspiratory to expiratory breathing, i.e., at the end of inspiration. This seems to be questionable in light of the decrease of inhaled particle mass with low flow rates (see Fig. 12). More accurately, it is the enhancement of momentary deposition efficiency (see Fig. 11), which may occur at the end of particle/vapor inspiration.

The total DF in the oral airways for cyclic inhalation is compared with those for steady inhalation considering different flow rates (Fig. 13). The best matching flow rate was determined to be the average between the mean and maximum flow rates, i.e., $Q_{\text{match}} = \frac{1}{2}(Q_{\text{mean}} + Q_{\text{max}})$. After segmental averaging, the DFs of nano-particles or vapor for cyclic inspiratory flow are not significantly different from that for constant flow with various matching flow rates, i.e., the errors range from −2% to +10%. In fact, the deposition result for steady matching flow (27.5%) is a good *conservative* estimate of the actual DF (26.9%). This conclusion is consistent with the experimental observations of Li et al. [14] for deposition of iodine vapor in a tracheobronchial cast. They observed relatively low depositions for cyclic flow and concluded that the cyclic inspiratory flow patterns do not cause a statistically significantly increase in the total deposition in the tracheobronchial region.

The momentary deposition patterns of $d_p = 1$ nm nano-particles or vapor during the inspiratory cycle are depicted in Fig. 14 in terms of the DEF (see DEF of Eq. (13)). The DEF contours vary little except at the beginning of inspiration ($t = T_1$) where deposition is minor after the inlet due to low convection. Because of large concentration gradients resulting in strong mixing, the highest deposition values almost always occur at the inlet for plug flow and uniformly distributed vapor. In addition, enhanced deposition may occur at the outer bend just after the soft palate or near the glottis. The deposition patterns during the major part of the inspiratory cycle resemble those for steady flow as well.

5.1.2.2. Deposition fractions of nano-particles. As discussed above, cyclic flow patterns have minor effects on nano-particle transport and deposition, hence, the following analysis considers only steady inhalation.

The variations of DF in the oral airway which is defined in Eq. (12), as a function of inhalation flow rate and particle diameter are depicted in Fig. 15. As expected, the DFs decrease with an increasing particle diameter because of the decrease in diffusive capacity (see Table 2). Similarly, the higher the inhalation flow rate, the lower the deposition of nano-particles because of reduced residence time. However, the inlet flow rate has a minor effect on particle deposition when compared to the influence of particle size. In fact, the deposition of 1 nm particles in the oral airway may be as high as 20–40% while the DFs of 150 nm particles may be as low as 0.01–0.05%.

A "diffusion parameter", Δ, considering the effects of inhalation flow rate, particle size and geometric features is usually employed to correlate the diffusional DF of nano-particles. It is defined as

$$\Delta = \frac{\pi \tilde{D} L}{4Q}, \tag{14}$$

where L is the length of the tube, and Q is the volumetric flow rate. A plot of DF in the oral airway model as a function of diffusion parameter Δ is provided in Fig. 16. All these scattered data can be correlated using the following equation:

$$\mathrm{DF}(\%) = \Delta^a \exp(b - c\Delta), \tag{15}$$

where $a = 0.69$, $b = 7.72$, $c = 86.3$ for $5 \times 10^{-8} < \Delta < 10^{-2}$ with $r^2 = 0.985$. As shown in Fig. 16, the inhalation flow rate has negligible effects on the DF when it is correlated with the diffusion parameter.

5.2. Steady transport and deposition of nano-particles in bifurcating airways

This section focuses on the steady airflow structures (Section 5.2.1) as well as nano-particle transport (Section 5.2.2) and deposition (Section 5.2.3) in the bronchial airway model representing Generations G0–G3 of Weibel's lung model where the inlet velocity profiles and turbulent quantities are adjusted from the trachea in the oral airway model.

5.2.1. Air flow structures

Considering inspiratory flow rate of $Q_{\mathrm{in}} = 15$ l/min, i.e., low-level breathing, Fig. 17 shows the mean-velocity fields in the planar triple-bifurcation airways which are physiologically 90° turned with respect to the

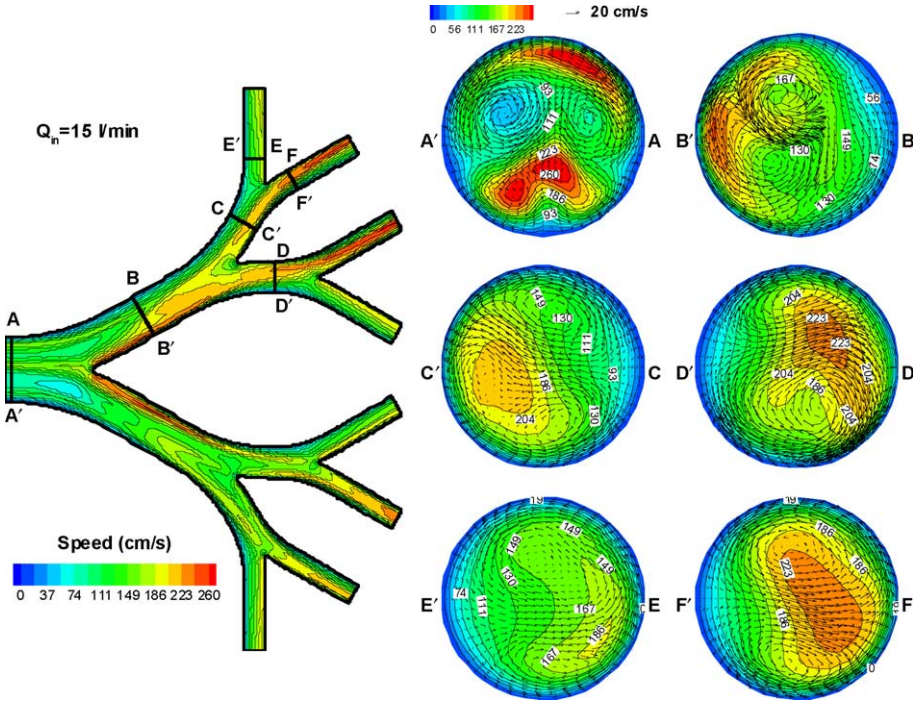

Fig. 17. Velocity profiles in the bifurcation airway model at steady inhalation with $Q_{\mathrm{in}} = 15$ l/min. The left panel exhibits mid-plane ($z = 0$ plane) speed contours. The right panel shows the axial velocity contours (magnitudes in cm/s) and secondary velocity vectors at different cross sections.

oral airways (see Figs. 1 and 6(a)). The selected cross-sectional views display the axial velocity contours as well as secondary velocity vectors. For such low-level breathing, the turbulent intensity is very low in the oral airway and flow instabilities cannot be induced in the bifurcating branches without any additional disturbances, which indicates that laminar flow prevails in this case. The inlet profiles for both axial and secondary velocities (see section A–A′) are fully three-dimensional, i.e., asymmetric about both the bifurcation and transverse planes. Two zones with high axial velocities exist at the upper and lower side of the tube (i.e., near the anterior and posterior walls of the trachea), and two strong secondary vortices appear at the tube center. The air stream splits at the first flow divider and a new boundary layer is generated at the inner wall of the first daughter tube. The skewed profile with a maximum axial velocity near the inner wall can be clearly observed at cross section B–B′. Another high-velocity region which appears near the upper side at section B–B′ may come from upstream. The locations and intensities of secondary vortices in the first daughter tube change as well, due to the centrifugal force effects when compared to those at the parent tube (A–A′). When the air stream continues to turn bends at the second and third daughter tubes, the velocity patterns vary with the development of upstream flows and the generation of the new boundary layers near the inner walls of the dividers. The different tubes may experience a different air flow rate as a result of skewed upstream velocity profiles (see section E–E′ and F–F′). Of interest is that the entrance effects become relatively weak in the second and third daughter tubes. That is, the asymmetry of axial and secondary velocities about the bifurcation plane (i.e., mid-plane or $z = 0$ plane) is lower in the second and third daughter branches (see sections C–C′, D–D′, E–E′ and F–F′) than in the first daughter and parent tubes (B–B′ and A–A′). The primary characteristics of the flow fields at cross sections C–C′, D–D′, E–E′ and F–F′ are quite similar; specifically: (i) skewed velocity profiles with the maximum velocity near the inner wall around the divider; and (ii) two distinct secondary vortices appearing at the upper and lower side of the tube, which moves the high speed fluid up around the top of the tube towards the outside of the bifurcation and low speed fluid from the outside of the bifurcation along the symmetry plane towards the inside of the bifurcation.

When the inspiratory flow rate is increased to 30 and 60 l/min, i.e., light activity and exercise breathing, the velocity profiles and the turbulent energy profiles change measurably in the oral airway part (see [45]). Subsequently, the velocity profiles at the entrance of the bronchial airway (cf. cross section A–A′ in Fig. 18) are different from those for $Q_{\text{in}} = 15$ l/min (Fig. 17). For the high flow rate cases, the velocity profiles become more blunt from the left (A′) to the right wall (A), and the maximum velocity zone moves to the top wall (i.e., the anterior wall of the trachea) at cross section A–A′ (see Fig. 17) with the occurrence of transition to turbulence after the glottis. The secondary motion decays and appears very weak at this cross section (A–A′). When the airstream turns the bend at the first divider, the maximum velocity region moves from the top wall to the inside wall of the bifurcation and secondary flow is re-established due to the centrifugal force effect. However, the entrance effects will again decrease in the daughter tubes of the second and third bifurcations. The axial velocities are almost symmetric about the bifurcation plane ($z = 0$ plane) at the cross sections E–E′ and F–F′ (see Fig. 18). In addition, the almost completely symmetric velocity profile at A–A′ about the transverse plane ($y = 0$ plane) results in quite similar velocity profiles in the lower and upper parts of the triple bifurcation split at the first flow divider.

Although the turbulence levels appear to decay approaching an asymptotic level of approximately $k/u_{\text{in}}^2 = 0.1$–0.2 at the inlet of bifurcating airways G0–G3, the flow instabilities may be induced again at the bifurcation region due to the significant geometric transition from the parent tube to the two daughter tubes. Fig. 19 shows the turbulence kinetic energy distributions in airways G0–G3 with an inspiratory flow rate of $Q_{\text{in}} = 60$ l/min. The strong turbulence fluctuations occur just around the flow dividers due to the contraction of top and bottom surfaces near the carinal ridges (see sections 1–1′, 3–3′ and 4–4′), and they then decay rapidly in the straight tubular segments. The turbulence intensities may be different at different dividers due to different upstream effects and contraction ratios. The maximum turbulent fluctuations may occur at the third inside divider (see 4–4′). In general, turbulence which occurs after the throat may propagate to at least Generation G3 even at a low local Reynolds number (say, $Re_{\text{local}} = 700$) because of the

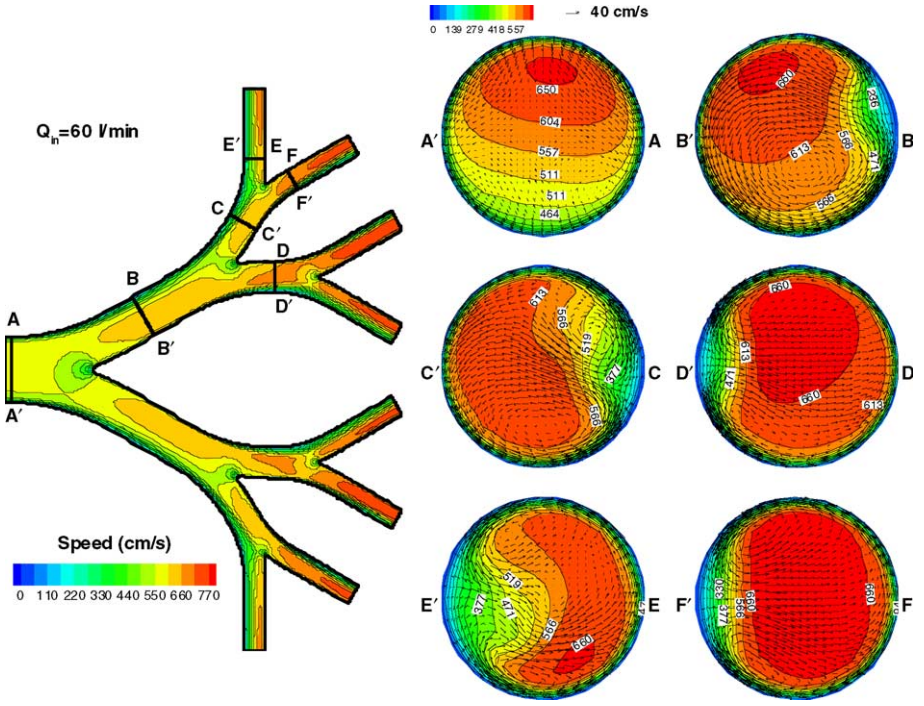

Fig. 18. Velocity profiles in the bifurcation airway model at steady inhalation with $Q_{in} = 60$ l/min. The left panel exhibits mid-plane ($z = 0$ plane) speed contours. The right panel shows the axial velocity contours (magnitudes in cm/s) and secondary velocity vectors at different cross sections.

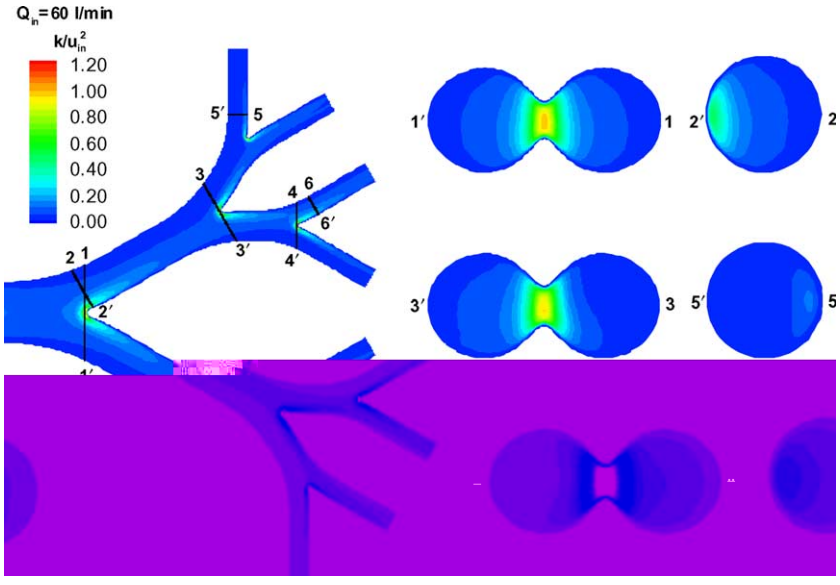

Fig. 19. Distributions of turbulence kinetic energy in the bifurcation airway model at $Q_{in} = 60$ l/min.

enhancement of flow instabilities just upstream of the flow divider. This phenomenon is similar to some experimental observations by Olson et al. [73,74] and West and Hugh-Jones [75]; but turbulent fluctuation initiated around the flow divider has never been demonstrated before.

5.2.2. Transport of nano-particles

Figs. 20(a), (b) and 21(a), (b) show the distributions of two sets of nano-particles (i.e., $d_p = 1$ and 10 nm) in terms of local particle mass fraction for the inhalation flow rates $Q_{in} = 15$ and 60 l/min. The associated velocity profiles are shown in Figs. 17 and 18. Clearly, for tiny particles (say, $d_p = 1$ nm) with a low inspiratory flow rate of $Q_{in} = 15$ l/min the axial velocity field is a good indicator of particle distributions (see Fig. 20(a)), i.e., high-velocity regions imply high-concentration regions for particles and *vice versa*. This is because convection mass transfer is quite strong in the high-velocity regions and particles can rapidly convect and mix. However, at high flow rates, the dispersion of particles at the entrance is not as swift, even for $d_p = 1$ nm particles, because of the decrease in residence times (see section A–A′ in Fig. 21(a)). In addition, the concentration gradients are larger in the shear layer along the inner walls of the bifurcations (see cross sections B–B′ to F–F′ in Figs. 20 and 21), which may indicate enhanced deposition at the inside wall around the flow divider. The larger size particles ($d_p = 10$ nm) cannot diffuse as rapidly and hence deposit not as much as the tiny particles ($d_p = 1$ nm), leaving high particle concentrations mostly in the lumenal areas. However, in the low-velocity regions (i.e., outside bifurcation zones, C, D′, E′ and F′), the relatively long residence times for particles help them to establish a relatively large mass-transfer zone, i.e., a low-concentration region. The role of secondary flows in nano-particle transport is not as pronounced as it is for micro-particles. Specifically, in some cases micro-particles can be swept out of the strong secondary vortices due to their inertia, and preferential ring areas of high concentrations are generated outside the secondary vortices (see [41]). In contrast, no apparent relationship between concentration distribution and secondary airflow motion is observed for nano-particles. This may be because the drag, which is directly related to fluid motion, is the dominant force for micro-particles, while Brownian motion caused by molecular collisions is the controlling mechanism for nano-particle dispersion.

5.2.3. Deposition of nano-particles

The local deposition patterns of nano-particles can be described in terms of the distribution of the DEF as given in Eq. (13). Fig. 22(a) and (b) depict the DEF-contours in the bifurcation airway model G0–G3. For both 1 and 10 nm particles, the enhanced deposition mainly occurs at the carinal ridges and the inside walls around the dividers due to the complicated air flows and large particle-concentration gradients in these regions. However, the maximum DEF-values vary with each bifurcation. The specific values of the maximum DEF-values in different bifurcations (see Fig. 1) for various pairs of flow rate and particle size are given in Table 4. Except for $Q_{in} = 15$ l/min and $d_p = 1$ nm, the maximum DEF-values increase with the sequential bifurcation for all other Q_{in}–d_p combinations. The exception for $Q_{in} = 15$ l/min and $d_p = 1$ nm at the first bifurcation is caused by a decrease in core particle concentration just upstream of the flow divider with the sequential bifurcation due to heavy deposition upstream (see Fig. 20(a)). In other cases, the increase of axial velocity in the tube center, upstream of the divider with the sequential bifurcation (cf. sections A–A′, B–B′ and D–D′ in Figs. 20 and 21), results in the increase of local mass transfer at the carinal ridge with the sequential bifurcation (i.e., B1, B2.1 and B3.2, Fig. 1), while the core concentrations just upstream of flow dividers vary little. The variation of DEF-values with sequential bifurcation also indicates that single or double bifurcation models are insufficient for investigating particle deposition in the bronchial airways. For 100 nm particles, the maximum DEF still occurs at the third carinal ridge; however, except at the entrance region, the DEF distribution tends to be more uniform. As a result, the maximum DEF for 100 nm particles is smaller than those for 1 and 10 nm particles. This is attributed to the decreasing diffusivities and more uniformly distributed concentration fields in the tubes (cf. Figs. 21 and 22) for larger nano-particles. Such a near-uniform distribution of deposited nano-particles also implies that more sites

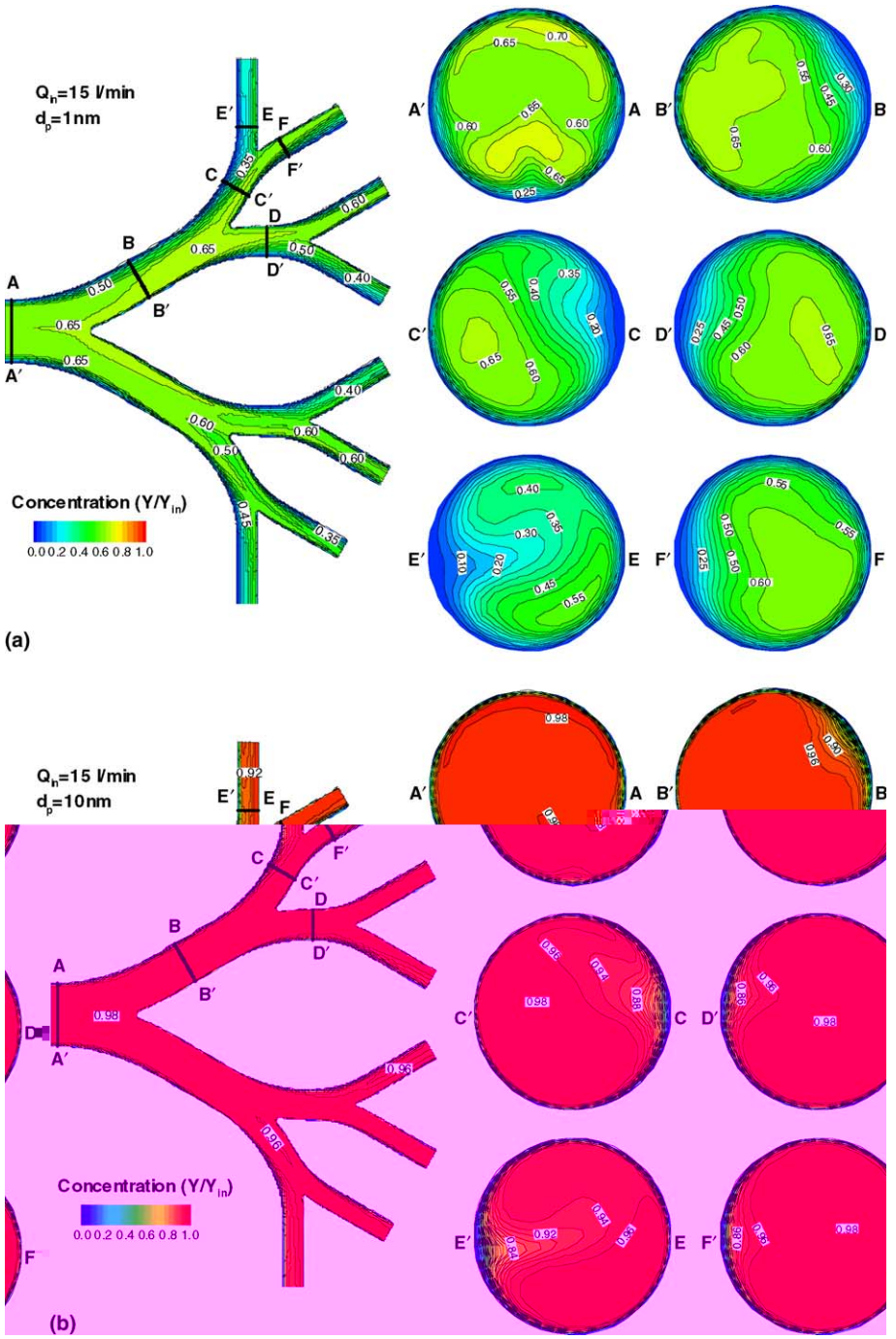

Fig. 20. Concentration contours in the bifurcation airway model for an inspiratory flow rate of $Q_{in} = 15$ l/min for nano-particles with diameters: (a) $d_p = 1$ nm; and (b) $d_p = 10$ nm.

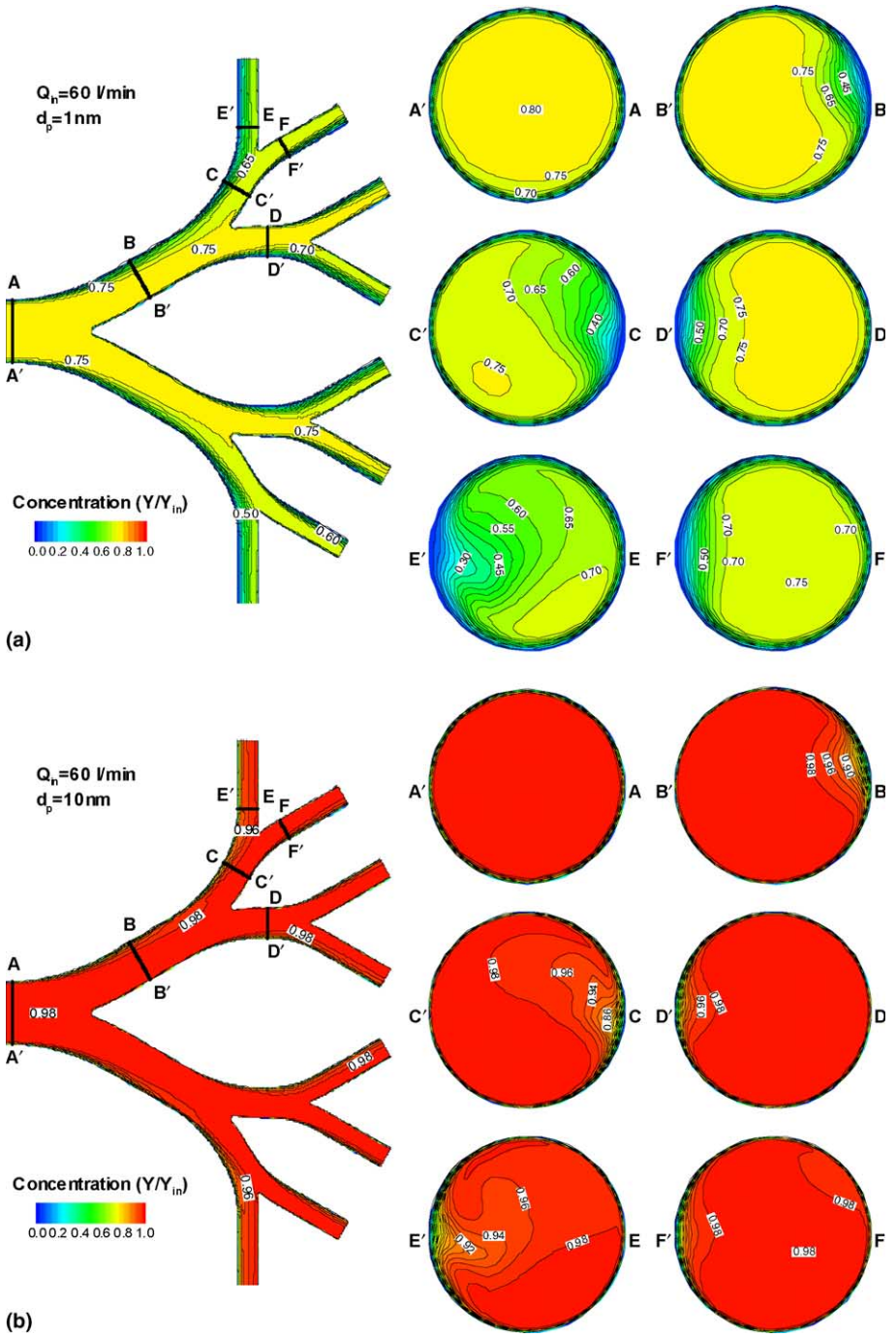

Fig. 21. Concentration contours in the bifurcation airway model for an inspiratory flow rate of $Q_{in} = 60$ l/min for nano-particles with diameters: (a) $d_p = 1$ nm; and (b) $d_p = 10$ nm.

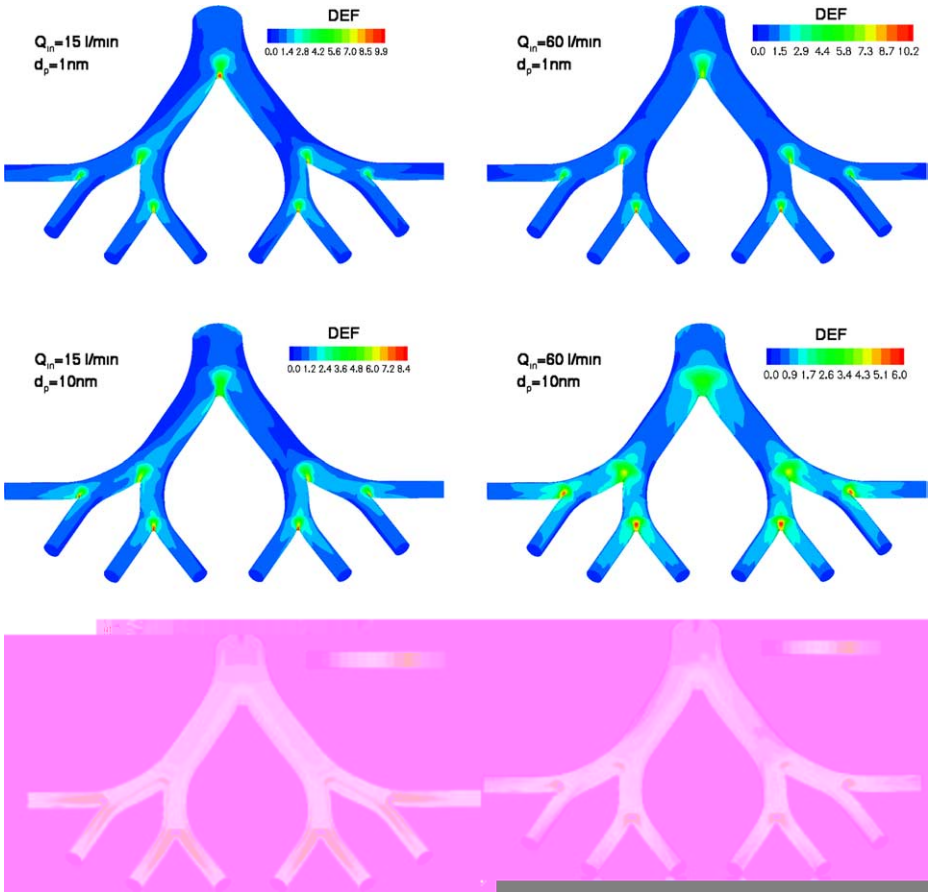

Fig. 22. 3-D distributions of the deposition enhancement factor (DEF) of nano-particles in the bifurcation airway model for steady inhalation with: (a) $Q_{in} = 15$ l/min; and (b) $Q_{in} = 60$ l/min.

Table 4
Maximum DEFs in different bifurcations

Bifurcation	First	Second	Third
$Q_{in} = 15$ l/min, $d_p = 1$ nm	9.86	8.81	9.55
$Q_{in} = 15$ l/min, $d_p = 10$ nm	5.04	6.53	8.36
$Q_{in} = 15$ l/min, $d_p = 100$ nm	1.62	2.29	3.23
$Q_{in} = 30$ l/min, $d_p = 1$ nm	7.45	8.27	10.31
$Q_{in} = 30$ l/min, $d_p = 10$ nm	4.24	5.27	7.11
$Q_{in} = 30$ l/min, $d_p = 100$ nm	1.35	1.92	2.70
$Q_{in} = 60$ l/min, $d_p = 1$ nm	7.31	8.19	10.22
$Q_{in} = 60$ l/min, $d_p = 10$ nm	3.40	4.51	5.98
$Q_{in} = 60$ l/min, $d_p = 100$ nm	1.22	1.73	2.46

Table 5
Comparison of total deposition fraction (%) in generations G0–G3 ($Q_{in} = 60$ l/min)

	Particle diameter (nm)								
	1	3	5	10	20	30	50	100	150
With turbulence	9.520	2.898	1.567	0.672	0.293	0.177	0.0846	0.0273	0.0142
Without turbulence	9.050	2.890	1.565	0.672	0.293	0.177	0.0845	0.0272	0.0141

may interact with cell membranes, hence there is a higher probability of transport of toxic substances into the tissue/blood domain.

As discussed before, turbulence exists at each bifurcation in generations G0–G3 at medium and high inlet flow rates. The effects of turbulent flow on nano-particles deposition are shown in Table 5 in terms of total DF in G0–G3 with $Q_{in} = 60$ l/min, where "without turbulence" implies $v_T = 0$ in Eq. (7). In contrast to micro-particles, the effect of turbulent fluctuations on nano-particle deposition is minor. The reason for this may be that the eddy viscosity (v_T) is very small in the near-wall regions, i.e., in the order of 10^{-7} to 10^{-10} cm^2/s. The local deposition patterns "without turbulence" also exhibit almost no change when compared with those "with turbulence", except the slight increase in the maximum DEF-value for 1 nm diameter particles.

To summarize the deposition data, Fig. 23 shows the DF-variations vs. particle diameter in the four-generation bronchial airway model. The DFs (see Eq. (12)) in an average four-generation airway as measured by Cohen et al. [13] are also given for comparison. It is seen that the simulated data agree well with the experimental data; again, validating the present CFPD simulation model. The trends of the relation between the DFs and particle size and inspiratory flow rates are the same as those for the oral airway model.

Fig. 24(a) and (b) show the DF-variations as a function of particle size across different bifurcations. The DF in each bifurcation is related to the local Reynolds number and bifurcation geometric features (e.g., total surface area, etc.) when the particle size is fixed. As a result, the DF in the third bifurcation is a little higher than that in the first and second bifurcations for the same-sized particles at the same inspiratory flow rate, while the DFs in the first and second bifurcations are almost the same. The DF is about the same for both branches of the third bifurcation as well (see Fig. 24(b)).

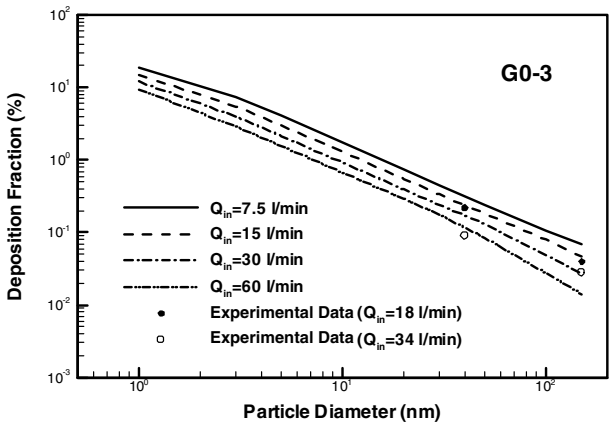

Fig. 23. Deposition fraction variations of nano-particles in the bifurcation airway model vs. flow rate and particle diameter. The experimental data were obtained from Cohen et al. [13].

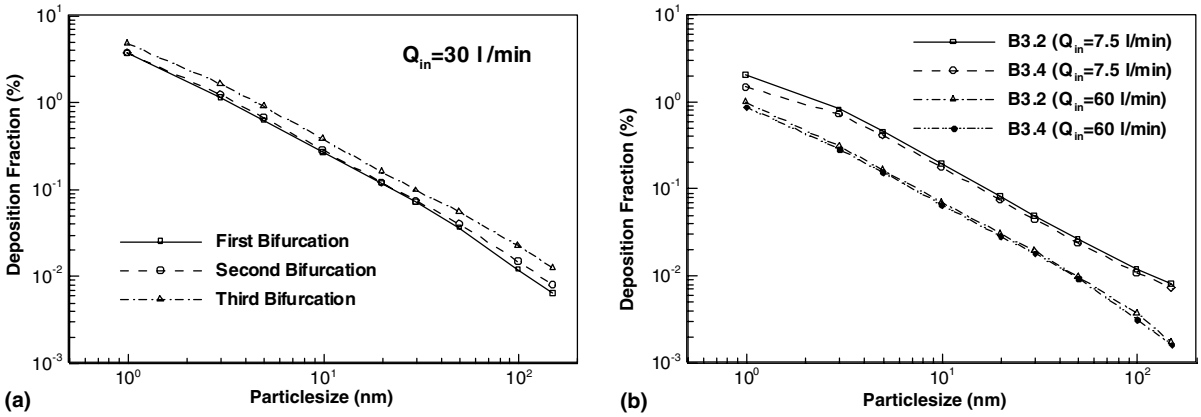

Fig. 24. Deposition fraction variations of nano-particles across different bifurcations in the bifurcation airway model.

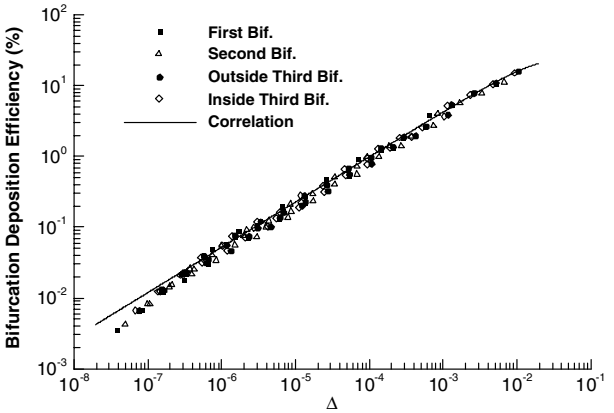

Fig. 25. Plots of deposition efficiencies of nano-particles for different model bifurcations versus the diffusion parameter Δ.

The DE data sets for individual bifurcations can be correlated with Δ of Eq. (15) where the coefficients are $a = 0.64$, $b = 5.84$, and $c = 16.75$, for $5 \times 10^{-8} < \Delta < 10^{-2}$ with $r^2 = 0.991$ (see Fig. 25). The bifurcation deposition efficiency is defined as the ratio of deposited mass at one individual bifurcation to the inhaled mass at the inlet of that bifurcation. For calculating Δ, the characteristic length L is defined as the ratio of the total surface area of the individual bifurcation to its parent tube diameter. As shown in Fig. 25, the DE may change slightly from generation to generation in the lung because of the strong variations in airway geometry. Clearly, the DE(Δ) correlation equation, which captures the general trend based on all our simulation data, would be most applicable for global (algebraic) lung modeling efforts.

6. Conclusions

The following conclusions can be drawn from the experimentally validated CFPD modeling results.

(1) Apparent effects of unsteadiness can be observed in the oral airways during the decelerating phase of the inspiratory cycle. Specifically, airflow during the decelerating phase exhibits apparent turbulent fea-

tures and resembles those at peak inspiration. The onset of turbulence may take place during acceleration when $Re_{\text{trachea}} \approx 2400$; but, turbulent fluctuations may not weaken until $Re_{\text{trachea}} < 800$ during deceleration. Moreover, the difference in pressure drops between the transient case and quasi-steady case is relatively large during deceleration.

(2) The dynamics of 1 nm particles can be similar to vapor transport and deposition because of equivalent diffusion parameters. Both the momentary deposition efficiencies and deposition patterns of these species remain almost constant during the major part of the inspiratory cycle. However, near the end of inspiration, the deposition efficiency increases with decreasing flow rate because of the increasing residence times for particles. At the end of inspiration, the enhancement of momentary deposition efficiency may occur for nano-particles, but the inhaled mass decreases with decreasing flow rate. The total DFs of nano-particles due to diffusional transport for cyclic inspiratory flow is not significantly different from that for constant flow with a matching flow rate because the deposition changes little from the mean flow rate case to the peak flow rate case.

(3) Turbulent fluctuations, which occur after the throat, propagate at least to Generation G3 at medium and high inspiratory flow rates due to the enhancement of flow instabilities just upstream of the flow dividers. However, the effects of turbulent fluctuations on nano-particle deposition are quite minor in the human upper airways.

(4) In a four-generation bronchial airway model (G0–G3), the entrance effects appear to weaken in the last two generations.

(5) Enhanced deposition of nano-particles mainly occurs at the carinal ridges and the inside walls around the cranial ridges. The maximum enhanced deposition ($\text{DEF}_{\max}$) is about 2.5–10 times of the average dose in the upper tracheobronchial airway model for $15 \leqslant Q_{\text{in}} \leqslant 60$ l/min and $1 \leqslant d_{\text{p}} \leqslant 150$ nm, which varies with bifurcation, particle size, and inhalation flow rate. The local deposition is more uniformly distributed for relatively large-size particles (say, $d_{\text{p}} = 100$ nm) than for small-size particles (say, $d_{\text{p}} = 1$ nm). Such a near-uniform distribution of deposited nano-particles also implies that more sites may interact with cell membranes, hence there is a higher probability of transport of toxic substances into the tissue/blood domain.

(6) The role of secondary flows on nano-particle transport is not as pronounced as for micro-particles. The concentration distributions for nano-size particles tend to be more uniform with increasing particle size in the upper airways.

(7) The regional deposition efficiencies of nano-particles in the size range of 1–150 nm can be correlated with the diffusion parameter Δ, incorporating the effects of inhalation flow rate, particle size, and geometric length scale.

In summary, this work may elucidate basic physical insight of nano-particle or vapor transport relevant to dosimetry-and-health-effect studies as well as for drug aerosol delivery analyses. The findings may also provide necessary information for toxicologic or therapeutic impact assessments.

Disclaimer – The views and conclusions contained herein are those of the authors and should not be interpreted as necessarily representing the official policies or endorsements, either expressed or implied, of the Air Force Office of Scientific Research or the US Government.

Acknowledgements

This effort was sponsored by the Air Force Office of Scientific Research, Air Force Material Command, USAF, under grant number F49620-01-1-0492 (Dr. Walt Kozumbo, Program Manager) and the National Science Foundation (BES-0201271; Dr. Gil Devey, Program Director). The US Government is authorized to reproduce and distribute reprints for governmental purposes notwithstanding any copyright notation thereon. The use of CFX software from ANASYS Inc. (Canonsburg, PA) and access to the SGI Origin

2400 workstation at the North Carolina Supercomputing Center (Research Triangle Park, NC) are gratefully acknowledged as well.

References

[1] P. Gehr, J. Heyder (Eds.), Particle–Lung Interaction, Marcel Dekker, New York, 2000.
[2] M.W. Frampton, Systemic and cardiovascular effects of airway injury and inflammation: ultrafine particle exposure in humans, Environ. Health Perspectives 109 (2001) 529–532.
[3] N. Singh, G.S. Davis, Review: occupational and environmental lung disease, Curr. Opin. Pulmonary Med. 8 (2002) 117–125.
[4] K. Donaldson, V. Stone, P.S. Gilmour, D.M. Brown, W. Macnee, Ultrafine particles: mechanisms of lung injury, Phil. Trans. R. Soc. Lond. A 358 (2000) 2741–2749.
[5] K. Donaldson, X.Y. Li, W. Macnee, Ultrafine (nanometer) particle-mediated lung injury, J. Aerosol Sci. 29 (1998) 553–560.
[6] P. Gehr, M. Geiser, V. Im Hof, S. Schürch, Surfactant-ultrafine particle interactions: what we can learn from PM_{10} studies, Phil. Trans. R. Soc. Lond. A 358 (2000) 2707–2718.
[7] G. Oberdörster, Pulmonary effects of inhaled ultrafine particles, Int. Arch. Occupat. Environ. Health 74 (2001) 1–8.
[8] K.H. Cheng, Y.S. Cheng, H.C. Yeh, D.L. Swift, Deposition of ultrafine aerosols in the head airways during natural breathing and during simulated breath-holding using replicate human upper airway casts, Aerosol Sci. Technol. 23 (1995) 465–474.
[9] K.H. Cheng, Y.S. Cheng, H.C. Yeh, R.A. Guilmette, S.Q. Simpson, Y.H. Yang, D.L. Swift, In vivo measurements of nasal airway dimensions and ultrafine aerosol deposition in the human nasal and oral airways, J. Aerosol Sci. 27 (1996) 785–801.
[10] K.H. Cheng, Y.S. Cheng, H.C. Yeh, D.L. Swift, Measurements of airway dimensions and calculation of mass transfer characteristics of the human oral passage, J. Biomech. Eng. – Trans. ASME 119 (1997) 476–482.
[11] K.H. Cheng, Y.S. Cheng, H.C. Yeh, D.L. Swift, An experimental method for measuring aerosol deposition efficiency in the human oral airway, Am. Ind. Hyg. Assoc. J. 58 (1997) 207–213.
[12] Y.S. Cheng, Y. Yamada, H.C. Yeh, D.L. Swift, Diffusional deposition of ultrafine aerosols in a human nasal cast, J. Aerosol Sci. 19 (1988) 741–751.
[13] B.S. Cohen, R.G. Sussman, M. Lippmann, Ultrafine particle deposition in a human tracheobronchial cast, Aerosol Sci. Technol. 12 (1990) 1082–1091.
[14] W. Li, J.Q. Xiong, B.S. Cohen, The deposition of unattached radon progeny in a tracheobronchial cast as measured with iodine vapor, Aerosol Sci. Technol. 28 (1998) 502–510.
[15] C. Kleinstreuer, Two-Phase Flow: Theory and Applications, Taylor & Francis, New York, 2003.
[16] G. Yu, Z. Zhang, R. Lessmann, Computer simulation of the flow field and particle deposition by diffusion in a 3-D human airway bifurcation, Aerosol Sci. Technol. 25 (1996) 338–352.
[17] G. Yu, Z. Zhang, R. Lessmann, Fluid flow and particle diffusion in the human upper respiratory system, Aerosol Sci. Technol. 28 (1998) 146–158.
[18] J.S. Kimbell, E.A. Gross, D.R. Joyner, M.N. Godo, K.T. Morgan, Application of computational fluid dynamics to regional dosimetry of inhaled chemicals in the upper respiratory tract of the rat, Toxicol. Appl. Pharmacol. 121 (1993) 253–263.
[19] G.M. Kepler, R.B. Richardson, K.T. Morgan, J.S. Kimbell, Computer simulation of inspiratory nasal airflow and inhaled gas uptake in a rhesus monkey, Toxicol. Appl. Pharmacol. 150 (1998) 1–11.
[20] I. Balásházy, W. Hofmann, Particle deposition in airway bifurcations. I. Inspiratory flow, J. Aerosol Sci. 24 (1993) 745–772.
[21] I. Balásházy, W. Hofmann, Deposition of aerosols in asymmetric airway bifurcations, J. Aerosol Sci. 26 (1995) 273–292.
[22] E.R. Weibel, Morphometry of the Human Lung, Academic Press, New York, 1963.
[23] B. Asgharian, S. Anjilvel, A Monte Carlo calculation of the deposition efficiency of inhaled particles in lower airways, J. Aerosol Sci. 25 (1994) 711–721.
[24] A. Moskal, L. Gradoñ, Temporary and spatial deposition of aerosol particles in the upper human airways during breathing cycle, J. Aerosol Sci. 33 (2002) 1525–1539.
[25] Z. Zhang, C. Kleinstreuer, Low Reynolds number turbulent flows in locally constricted conduits: a comparison study, AIAA J. 41 (2003) 831–840.
[26] W. Hofmann, R. Golser, I. Balásházy, Inspiratory deposition efficiency of ultrafine particles in a human airway bifurcation model, Aerosol Sci. Technol. 37 (2003) 988–994.
[27] CH. Brücker, W. Schröder, Flow visualization in a model of the bronchial tree in the human lung airways via 3-D PIV, in: Proceedings of PSFVIP-4, June 3–5, Chamonix, France, 2003.
[28] C. Caro, R.C. Schroter, N. Watkins, S.J. Sherwin, V. Sauret, Steady inspiratory flow in planar and non-planar models of human bronchial airways, Proc. R. Soc. Lond. A 458 (2002) 791–809.
[29] H.K. Chang, Flow dynamics in the respiratory tract, in: H.K. Chang, M. Paiva (Eds.), Respiratory Physiology: An Analytical Approach, Marcel Dekker, Inc, New York, 1989, pp. 57–138.

[30] J.K. Comer, C. Kleinstreuer, Z. Zhang, Flow structures and particle deposition patterns in double bifurcation airway models. Part 1. Air flow fields, J. Fluid Mech. 435 (2001) 25–54.
[31] H. Fujioka, K. Oka, K. Tanishita, Oscillatory flow and gas transport through a symmetrical bifurcation, J. Biomech. Eng. 123 (2001) 145–153.
[32] B. Gatlin, C. Cuicchi, J. Hammersley, D. Olson, R. Reddy, G. Burnside, Computational simulation of steady and oscillating flow in branching tubes, in Bio-Medical Fluids Engineering, ASMEFED vol. 212, 1995, pp. 1–8.
[33] B.B. Lieber, Y. Zhao, Oscillatory flow in a symmetric bifurcation airway model, Ann. Biomed. Eng. 26 (1998) 821–830.
[34] Y. Liu, R.M.C. So, C.H. Zhang, Modeling the bifurcating flow in an asymmetric human lung airway, J. Biomech. 36 (2003) 951–959.
[35] N. Nowak, P.P. Kakade, A.V. Annapragada, Computational fluid dynamics simulation of airflow and aerosol deposition in human lungs, Ann. Biomed. Eng. 31 (2003) 374–390.
[36] T.J. Pedley, R.C. Schroter, M.F. Sudlow, Flow and pressure drop in systems of repeatedly branching tubes, J. Fluid Mech. 46 (1971) 365–383.
[37] A. Ramuzat, M.L. Riethmuller, PIV investigations of oscillating flows with a 3D lung multiple bifurcation model, in: 11th Int. Symp. on Appl. of Laser Techniques to Fluid Flows, Lisbon, Portugal, June 13–16, 2002, paper 19-1.
[38] R.C. Schroter, M.F. Sudlow, Flow patterns in models of the human bronchial airways, Respir. Physiol. 7 (1969) 341–355.
[39] B. Snyder, D.E. Olson, Flow development in a model airway bronchus, J. Fluid Mech. 207 (1989) 379–392.
[40] G. Tanaka, T. Ogata, K. Oka, K. Tanishita, Spatial and temporal variation of secondary flow during oscillatory flow in model human central airways, J. Biomech. Eng. 121 (1999) 565–573.
[41] Z. Zhang, C. Kleinstreuer, Transient airflow structures and particle transport in a sequentially branching lung airway model, Phys. Fluids 14 (2002) 862–880.
[42] T.J. Pedley, Pulmonary fluid dynamics, Ann. Rev. Fluid Mech. 9 (1977) 229–274.
[43] J.B. Grotberg, Pulmonary flow and transport phenomena, Ann. Rev. Fluid Mech. 26 (1994) 529–571.
[44] J.B. Grotberg, Respiratory fluid mechanics and transport processes, Ann. Rev. Biomed. Eng. 3 (2001) 421–457.
[45] C. Kleinstreuer, Z. Zhang, Laminar-to-turbulent fluid-particle flows in a human airway model, Int. J. Multiphase Flow 29 (2003) 271–289.
[46] T.E. Corcoran, N. Chigier, Characterization of the laryngeal jet using phase doppler interferometry, J. Aerosol Med. 13 (2000) 125–137.
[47] T. Gemci, T.E. Corcoran, N. Chigier, A numerical and experimental study of spray dynamics in a simple throat model, Aerosol Sci. Technol. 36 (2002) 18–38.
[48] I.M. Katz, T.B. Martonen, Flow patterns in three-dimensional laryngeal models, J. Aerosol Med. 9 (1996) 501–512.
[49] I.M. Katz, T.B. Martonen, A numerical study of particle motion within the human larynx and trachea, J. Aerosol Sci. 30 (1999) 173–183.
[50] W.I. Li, M. Perzl, G. Ferron, R. Batycky, J. Heyder, D.A. Edwards, The macrotransport properties of aerosol particles in the human oral-pharyngeal region, J. Aerosol Sci. 29 (1998) 995–1010.
[51] W.I. Li, M. Perzl, J. Heyder, R. Langer, J.D. Brain, K.H. Englmeier, R.W. Niven, D.A. Edwards, Aerodynamics and aerosol particle deaggregation phenomena in model oral-pharyngeal cavities, J. Aerosol Sci. 27 (1996) 1269–1286.
[52] K.W. Stapleton, E. Guentsch, M.K. Hoskinson, W.H. Finlay, On the suitability of k–ϵ turbulence modeling for aerosol deposition in the mouth and throat: a comparison with experiment, J. Aerosol Sci. 31 (2000) 739–749.
[53] Z. Zhang, C. Kleinstreuer, C.S. Kim, Micro-particle transport and deposition in a human oral airway model, J. Aerosol Sci. 33 (2002) 1635–1652.
[54] C. Renotte, V. Bouffioux, F. Wilquem, Numerical 3D analysis of oscillatory flow in the time-varying laryngeal channel, J. Biomech. 33 (2000) 1637–1644.
[55] H. Shi, C. Kleinstreuer, Z. Zhang, C.S. Kim, Nano-particle transport and deposition in bifurcating tubes with different inlet conditions, Phys. Fluids, 2004, submitted for publication.
[56] T. Martonen, Z. Zhang, Y. Yang, Particle diffusion from developing flows in rough-walled tubes, Aerosol Sci. Technol. 26 (1997) 1–11.
[57] K. Horsfield, G. Dart, D.E. Olson, G.F. Filley, G. Cumming, Models of the human bronchial tree, J. Appl. Physiol. 31 (1971) 207–217.
[58] C.G. Philips, S.R. Kaye, On the asymmetry of bifurcation in the bronchial tree, Respir. Physiol. 107 (1997) 85–98.
[59] W.O. Fenn, H. Rahn, Handbook of Physiology, Sections 3: Respiration, American Physiological Society, Washington, DC, 1965.
[60] D.C. Wilcox, Turbulence Modeling for CFD, DCW Industries, Inc, LA Canada, CA, 1993.
[61] D. Shepard, A Two-dimensional interpolation function for irregularly-spaced data, in: Proc. 23rd National Conference ACM, ACM, 1968, pp. 517–524.
[62] AEA Technology, CFX-4.4: Solver (CFX International, Oxfordshire, UK, Now ANASYS, INC., Canonsburg, PA, 2001).
[63] W.H. Finlay, The Mechanics of Inhaled Pharmaceutical Aerosols: An Introduction, Academic Press, London, UK, 2001.

[64] J.B. Gustafson, J.G. Tell, D. Orem, Selection of Representative TPH Fractions Based on Fate and Transport Consideration, Amherst Scientific Publishers, Amherst, MA, 1997.
[65] I. Balásházy, W. Hofmann, T. Heistracher, Computation of local enhancement factors for the quantification of particle deposition patterns in airway bifurcations, J. Aerosol Sci. 30 (1999) 185–203.
[66] I. Balásházy, W. Hofmann, T. Heistracher, Local particle deposition patterns may play a key role in the development of lung cancer, J. Appl. Physiol. 94 (2003) 1719–1725.
[67] B.J. Fan, Y.S. Cheng, H.C. Yeh, Gas collection efficiency and entrance flow effect of an annular diffusion denuder, Aerosol Sci. Technol. 25 (1996) 113–120.
[68] R.I. Issa, Solution of the implicitly discretised fluid flow equations by operator splitting, J. Comput. Phys. 62 (1986) 40–65.
[69] Z. Zhang, C. Kleinstreuer, Species heat and mass transfer in a human upper airway model, Int. J. Heat Mass Transfer 46 (2003) 4755–4768.
[70] D.B. Ingham, Diffusion of aerosols in the entrance region of a smooth cylindrical pipe, J. Aerosol Sci. 22 (1991) 253–257.
[71] C.S. Kim, Ultrafine particle deposition in a double bifurcation tube with human G3–G5 airway geometry (US EPA, Internal Report, 2002).
[72] T.J. Pedley, R.C. Schroter, M.F. Sudlow, Gas flow and mixing in the airways, in: J.B. West (Ed.), Bioengineering Aspects of the Lung, Marcel Dekker Inc, New York, 1977, pp. 163–265.
[73] D.E. Olson, G.A. Dart, G.F. Filley, Pressure drop and fluid flow regime of air inspired into the human lung, J. Appl. Physiol. 28 (1970) 482–494.
[74] D.E. Olson, M.F. Sudlow, K. Horsfiled, G.F. Filley, Convective patterns of flow during inspiration, Arch. Intern. Med. 131 (1973) 51–57.
[75] J.B. West, P. Hugh-Jones, Patterns of gas flow in the upper bronchial tree, J. Appl. Physiol. 14 (1958) 753–759.